n-WALL

Present and Future

Zoltán Seres

KFKI RMKI, Budapest, Hungary

NSCL MSU, East Lansing, USA

(March 10, 2000)

Abstract

The precise time calibration of the n-WALL is demonstrated using the laser synchronization method. The position dependence of the energy calibration is discussed and corrected. The neutron detection efficiency is studied. The pulse shape discrimination is investigated using different charge measuring circuits. Recommendation is given for set up and on-line calibration of the wall. The software tools are reviewed supporting the calibration, the test and effective usage of the wall.

1. PREFACE

The motivation of writing this summary report on the n-WALL is the long break of the NSCL accelerators. I feel myself to be responsible for working the n-WALL. I think I must summarize our experiences operating the wall before we forget them.

It turned out in the last experiment that there is no standard procedure getting work the wall. We are improvising reconstructing some sets of spectra skipping very important basic steps. That's why in the last experiment I began to beleive that the wall went wrong. No! The n-WALL is really a

very nice detector but we are using it rather occasionally not properly. I have suggested already certain sequence of procedures starting the wall [1], sequence of calibration steps and set of informative spectra which can be prepared in advance, for one cannot improvise in the rush of starting the experiment. There must be a mandatory standard starting procedure.

The second reason is that I am convinced that we do not use the ultimate power offered by the detector. In the offline time and energy calibration I have found very remarkable fine effects which improve the characteristics of the wall and even convinced me about its perfect working.

With this paper I should like to provocate criticism and inititate new ideas.

2. INTRODUCTION

The neutron wall is a large area position sensitive neutron detector with possible small scattering material compared to the sensitive volume. The neutron wall was planned basically for experiments with radioactive beams.

In the radioactive beam experiments there are no γ-rays or only a few of them making difficult the time calibration. Therefore the n-WALL is equipped with a laser light triggering system helping the synchronization of the PMT-s and supporting the timing set up of the electronics.

Because of the large volume of the scintillator the n-WALL has a relatively large cosmics background cca. 350 counts/s per cell. Therefore the pulse shape discrimination has vital importance to separate the neutron detections from the cosmic γ-rays, electrons and μ-mesons.

In this report we perform an advanced calibration of the n-WALL, summarize the experience in setting the electronics and review the software tools. Finally we suggest a mandatory setting up and calibration process of the wall.

The calibration below was performed in April 1999 using the data measured by the electronic setup used in experiment NSCL #98016. The time calibration was made with laser synchronization and a new procedure is discussed in section 3 allowing common time base for all cells using one parameter to be fitted.

The position dependence of the energy calibration is studied in section 4 making possible the correction. The neutron detection efficiency of the cells is compared to the old type CAN detector in section 5. The pulse shape discrimination is improved and was tested with different faster QDC units in section 6. The main points of setting the electronics are summarized in section 7, and the software tools are given in section 8.

The algorithms and notations used in the paper are summarized in Appendix I. The calibration constants are given in Appendix II. A mandatory starting and calibration process is recommended in Appendix III. The introductory comments and the calling sequences of the auxiliary programs are collected in Appendix IV.

3. TIME CALIBRATION, REHABILITATION OF THE LASER

The energy of the neutrons is determined by their time of flight measured between the timing of the PMT-s and the stop signal produced from the fragment detection. In the time calibration one has to measure the time unit of the measuring circuit and determine the delay of the individual PMT-s and the stop signal. The PMT delay involves the time of flight of the light in the cell, the transit time through the PMT, the cable delays and the delay in the CFD and TFC input circuit. The time calibration usually is performed taking the promt γ-ray peak if exists.

In radioactive beam experiments there are a few if any promt γ-rays giving

a reference time point in the cells. Therefore for synchronization of the PMT-s the light of a nitrogen UV (337 nm) laser is ejected to the center of every cell through quarz fibers of uniform length. The time is measured to the stop signal of a reference detector. The individual PMT delays are eliminated by the laser synchronization i.e. by measuring the time related to the laser time peak and only one delay, the delay of the stop signal has to be determined.

It turned out, however, that there is a rather serious cross talk between the electronic channels. To avoid the cross talk the pulses from the left and right PMT-s of the cells are fed into separate chain of 16 channel units. The laser pulses, however, appear simultainously and the cross talk is inevitable and may result about 20 ns shift in timing of every PMT. Therefore the laser synchronization was dropped and the laser peak was used only for the calibration of the channel width of the TFC-FERA chain with a series of 9 stop delay steps and *the PMT delay was estimated by an arbitrary time zero determined individually for every PMT* resulting in symmetric ± 100 cm cosmic ray distributions. The TFC charge is measured by a FERA with automatic pedestal subtraction and overflow supression. The pedestals must be exact values for an erronous pedestal value gives a position shift and timing error.

For the laser synchronization — in order to eliminate the cross talk — the PMT-s of one cell have to be biased individually at once. Therefore a program was developed which gives the high voltage to the PMT-s automatically pair wisely cell by cell for a given time. In case of individual supplying the high voltage the cross talk appears clearly in the neighbouring channels up and down. The time channel is started but there no charge belongs to it so the cross talk can be identified. The cross talk is demonstrated in fig 1. The measured left time is plotted versus the geometric mean of the total charge in cell 2. The real peak around $sqtt = 1500$ and $Time = 980$ belongs to the

PMT of cell 2 biased while the peak at zero charge and $Time = 890$ channel comes from cross talk when the cell 3 is biased. The time shift of the cross talk peak corresponds to a delayed start pulse of about 20 ns characteristic for the channel. The appearance of the cross talk depends on the amplitude. Laser pulses of about $qtot = 1000$ channel give a cross talk time pulse in 100% of the events upto a CFD discrimination level of 10×5.5 mV. To localize the source of the cross talk the HV was supplied to PMT 1. The cross talk appeared in channel 2. The cables of PMT 2 and 16 were interchanged at the input of the dynode patch panel, and the cross talk remained in channel 2. Then the outputs 2 and 16 of the dynode patch panel were swapped, and the cross talk remained also in channel 2. Then the outputs of the CFD 2 and 16 were swapped at the input of the TFC and the cross talk went through to the 16^{th} channel. So very probably the LeCroy 3420 CFD is responsible for the cross talk although the manual gives for the cross talk $< 5\%$. The delay of the CFD is 15+10 ns which is close to the measured time shift supporting the assumption that probably the front of the output pulse starts the neighbouring channels.

In individual HV supply mode the PMT-s can be synchronized taking the laser time peak measured with a reference stop detector see fig. 2. The time resolution is 0.7 ns FWHM. Using the laser peak position T_{i0} and the channel width dt_i the measured T_i can be calibrated in 200 ps unit for every PMT:

$$t_i = 5(T_i + \delta - T_{i0})dt,$$

where δ is a random number between 0 and 1. The time t_i is free from the PMT transit time, cable and electronics timing delays, it contains only the time of flight of the light through half of the cell and the stop delay which are common for all cells and it is not sensitive for the pedestal error. The average of the left and right time measured with an outer stop signal is position

independent. The time of flight difference of the light is compensated, the time is reduced to the middle of the cell, and can be used for timing. In case of neutron single mode the stop pulse is correlated, the self stop spectrum corresponds to the dynamic range of the half cell length (≈ 7 ns).

The position is determined from the left–right difference of the time of flight of the light in the cell:

$$x_k = (t_{kR} - t_{kL})v_{eff}/5.$$

The effective light velocity in the cell was measured earlier [2] with collimated ^{60}Co and ThC" sources shown in fig 3. In the 7^{th} cell of the second wall the avarage $\frac{dx}{dT} = 0.379$ was measured which with the channel width $\frac{dt}{dT} =$ 46.97 ps/ch gives $v_{eff} = \frac{dx}{dt} = 7.83$ cm/ns. This value gives for the length of the cell 200 cm ($-100 \leq x < 100$ cm). The position resolution is about 5.5 cm FWHM for 5 MeVee pulses as shown in fig. 4.

The time calibration was checked by the position spectra of laser peak sitting on the cosmics background measured with individual biasing. Figure 5 shows that the cosmics background is shifted to the left about 6 cm. This shift was the argument why the laser synchronization method was dropped. We entrust in the laser measurement and we claim that changing the value of the channel widths dt_L and dt_R the cosmics position distribution becomes symmetric. The spectrum is the sum of coincidence events (laser) and downscaled neutron single events (cosmics). The coincidence spectrum is:

$$\frac{x}{v_{eff}} = (T_R - T_{R0})dt_R - (T_L - T_{L0})dt_L + (\delta_1 dt_R - \delta_2 dt_L),$$

while the cosmics spectrum has a common $\Delta t = \Delta T_R dt_R = \Delta T_L dt_L$ stop delay relative to the reference detector stop:

$$\frac{x}{v_{eff}} = (T_R - T_{R0})dt_R - (T_L - T_{L0})dt_L + (\Delta T_R dt_R - \Delta T_L dt_L) + (\delta_1 dt_R - \delta_2 dt_L).$$

For the laser $x \equiv 0$ independently from the dt-s for $T_R = T_{R0}$ and $T_L = T_{L0}$ per definitionem. The average of the last members and the third member in the last equation should be zero if the time calibration is correct. The error of the time calibration results in the expansion or shrinkage of the position range and a position shift because of the arbitrary stop delay. The cosmics distribution can be shifted to the left with dt_R smaller or dt_L larger and to the right by dt_R larger or dt_L smaller while the laser peak remains in zero. The question is what is the error of the measured channel width ($dt \approx 200$ ps). The lower panel of fig. 5 shows the corrected spectrum changing the value of the channel widths dt_L and dt_R by maximum 0.3% i.e. ± 0.6 ps/channel and the cosmics position distribution became symmetric. We calibrated all the cells tuning the channel width symmetrically on both sides for we do not have any reason to change one side which is equally good and is well inside the error of the channel width measurement.

The data taking has several modes. The PMT-s fireing starts the time measurement and *i)* a coincidence fragment pulse will stop them. If there is no fragment detected the event will be rejected or *ii)* as a downscaled neutron single event will be stopped by the delayed leader PMT pulse. *iii)* In case of laser calibration the fragment pulse is substituted by the laser reference detector. The self stop pulse is delayed that the leader self stop peak should be at the top of the TFC range. The upper limit is 1920 channel and the self stop peak is set into around 1800 channel having about 60 channels delayed tail. The coincidence stop is delayed so that the fastest particles, the promt γ peak should be well below the self stopped events i.e. about 1500 channel which determines the dynamic range $1500dt \approx 300$ ns. This peak has to be determined for the absolute time calibration of the time of flight. The laser reference stop pulse has an arbitrary delay putting the laser peak into the middle of the TFC range around 1000 channel. So the above ΔT-s are

about 700-780 channel shown in fig. 6 which magnify the effect of the dt errors ensuring a very sensitive tool for tuning the time calibration.

In summary the laser pulse — with individual biasing — can be used for precise synchronization of the PMT-s, it gives a reference time T_{i0} and fine tuning possibility for the dt_i channel width given in Appendix II. This allows to collect a summed γ-ray spectrum for all the cells which has probably an avaluable promt γ peak giving the absolute time calibration.

The time resolution measured with the laser pulses agrees with one of the self stop peak in n-single mode shown in fig. 6. It is characteristics for the banks: typical 0.8, 0.8, 0.6, and 1.2 ns FWHM for bank 1, 2, 3, and 4, respectively. In the banks 1, 2, and 4 the peaks are rather broad, double structured in the laser and self stop spectra as well referring to an instability of the starting side (CFD, TFC or FERA).

As a merit of the laser calibration can be mentioned that it called the attention to the cross talk of the electronics.

4. CHARGE MEASUREMENT, ENERGY CALIBRATION

The knowledge of the energy deposit is necessary for the efficiency estimation, for setting the software discrimination level, for checking the neutron scattering cross talk, and for the pulse shape discrimination.

The energy loss in the cell is measured by the charge produced at the anode of the PMT for the light collected at the ends of the cell. The light is guided by the total reflection on the outer wall of the glass cell, so the collection efficiency depends on the position of the emission because of the absorption, reflection loss and solid angle of the collection.

The light detected at the ends of the cells depends on the position. If the attenuation of the light is exponential the geometric mean of the charges

measured on the two ends is position independent and in first approximation measures the energy deposit.

$$\hat{q} = \sqrt{q_0 e^{-\frac{x}{\lambda}} \cdot q_0 e^{-\frac{L-x}{\lambda}}} = q_0 e^{-\frac{L}{2\lambda}},$$

where $L = 200$ cm the length of the cell and λ is the absorption length.

In the geometric mean calculation very important is the correct subtraction of the pedestals of the charge measuring QDC and FERA units.

$$\hat{q} = \sqrt{(Q_L - P_L)(Q_R - P_R)}.$$

A residuum of the pedestal introduces a nonlinear distortion.

The best way of the pedestal measurement is the accidental triggering interchanging the dynode patch panel outputs of the first and second wall not touching the QDC and FERA input units. New pedestal values are given in the MSU.LEX file (Appendix II.). Especially the FERA pedestals differ from the earlier values.

The pulse shape discrimination is in the first approximation position independent using the geometric mean values of the total and fast component charge values. The separation line can be fitted through the valleys between the neutron and γ peaks in the *sqft* fast component spectra measured with narrow *sqtt* total charge windows. In fig. 7 some *sqft* spectra and a second order polynomial fit is shown. This is apropriate for the low energy source calibration but for the high energy region it is better to use a quadratic polynomial extrapolated linearly which can be checked with the cosmics γ type spectra.

The geometric mean of the total charge can be calibrated for the energy deposit. The energy calibration is made producing the γ-ray spectra of ^{60}Co, ThC", and PuBe sources with a central position cut of ± 10 cm. A second order polynomial is fitted through the origo and the Compton edges (1.04, 2.38, and 4.2 MeV) giving the energy *Eeeq* in MeVee.

Figure 8 shows the position dependence of the left and right charges measured for PuBe source with position cuts and for collimated ^{60}Co source [2]. The charges are not pure exponential functions of the position, rather can be fitted by an exponential function superimposed on a constant background or far value. Therefore the geometric mean depends also on the position, it is constant only in the middle half of the cell see fig. 9. The function is similar for other cells and for the fast component too and its character seems to be general independent on cell and energies giving $\lambda \approx 73$ cm and $q(\frac{L}{2}) \approx 1.55q(L)$. We expect the opening of the solid angle at the ends but not along 60 cm.

The light collection can be modeled replacing the rectangular (7.7×6.4 cm^2) cross section cell with a round tube of radius r and one can count the number of reflections of the light originating along the axis at a distance x from one end. The light colledted at one end of the cell taking into account the light absorption:

$$S_L(x) = S \sum_{k=0}^{n} \Omega_k(x) P^k e^{-\frac{l_k(x)}{\lambda}},$$

where S is the light produced at x distance from the end of the cell, $\Omega_k(x)$ is the weight factor, the solid angle of the light suffering k reflections, P is the reflection coefficient in a *total reflection* process, λ is the absorption length in the liquid, $l_k(x)$ is the light path in case of k reflections, and n is the maximum number of reflections at x.

The photocathode (r_0) of the PMT is coupled to the cell by a taped plexi glass light pipe. Taking into account the length of the light pipe (x_0),

$$\Omega_0(x) = \frac{r_0^2 \pi}{4(x+x_0)^2 \pi},$$

$$\Omega_k(x) = \frac{r^2}{4(\frac{x+x_0}{2k+1})^2} - \frac{r^2}{4(\frac{x+x_0}{2(k-1)+1})^2} = 2k(\frac{r}{x+x_0})^2.$$

For k reflections the axial distance 2ξ and the light path $2l$ between two

reflections:

$$2\xi = \frac{x + x_0 - \xi}{k} \qquad \xi = \frac{x + x_0}{2k+1},$$

$$l = \sqrt{r^2 + \xi^2} = \sqrt{r^2 + (\frac{x + x_0}{2k+1})^2}, \quad \text{and} \quad l_k(x) = (2k+1)l.$$

The maximum number of reflections $k = n$ corresponds to ϑ_c critical angle of total reflections by $\xi_n = r \tan \vartheta_c$

$$n = \frac{x + x_0 - r \tan \vartheta_c}{2r \tan \vartheta_c}.$$

The taped light guide and the rounded end of the cell makes additional losses mainly in the photons arriving steeply under an angle around ϑ_c at the last, the n^{th} reflections. Therefore let us introduce a new reflection coefficient for the last reflection in case of n reflections: $P_n \ll P$. Supposing further that $r_0 \approx r$ the light collected:

$$\begin{aligned} S_L(x) = 2S(\frac{r_0}{x + x_0})^2 \frac{1}{8} e^{-\frac{\sqrt{r^2 + (x+x_0)^2}}{\lambda}} \\ + 2S(\frac{r}{x + x_0})^2 \sum_{k=1}^{n-1} k P^k e^{-\frac{\sqrt{(2k+1)^2 r^2 + (x+x_0)^2}}{\lambda}} \\ + 2S(\frac{r}{x + x_0})^2 n P^{n-1} P_n e^{-\frac{\sqrt{(2n+1)^2 r^2 + (x+x_0)^2}}{\lambda}}. \end{aligned}$$

The light collected from the knot points which are at round number of total reflections is calculated for $r_0 = r = 3.5$ cm, $\vartheta_c = 41.5^o$, $x_0 = 3.8$ cm, $P_n = 0.6$, $\lambda = 180$ cm, with P=0.88 as shown in fig. 10. The attenuation function is not pure exponential one. The reflections are decisive in the attenuation which explains the relative large far value similar to the measured one. The near value can be supressed by P_n. Because of the attenuation function the geometric mean depends also on the position see fig. 11.

The character of the measured geometric mean functions (see fig. 9) is well reproduced. The measured position dependence of geometric mean can be fitted by a second order polynomial and — according to the above model — the nonlinearity depends only on the geometry and optical properties of

the cell, and probably can be taken common to all cells which makes possible a correction on position reducing the charge to the central value (which is already calibrated *Eeeq* in MeVee):

$$cqtt = sqtt(1 - c_2x^2).$$

Figure 12 and 13 show the PuBe γ-ray spectrum and the scatter plot versus the position without and with position correction: *sqtt* and *cqtt*, respectively.

The position spectrum depends on the actual thresholds of the PMT-s, if the HV setting is not balanced the position spectrum is asymmetric as shown in fig. 14, however, setting the software cut in the *Eeeq* high enough that the software side cut should be higher than the hardware discrimination level, the position spectrum becomes symmetric.

The position correction improves a little the pulse shape discrimination too, which is shown in fig. 15 by the geometric means of the fast components $sqft$ gated by narrow *sqtt* window and the corrected $cqft$ and *cqtt* as well.

In summary the energy deposit must be measured and calibrated by the position corrected geometric mean of the charges. The hardware threshold has to be set so low that the software threshold set in the geometric mean should not been cut by neihter PMT-s. The optimal setting corresponds to a symmetric one therefore very important is the fine tuning of the PMT high voltages resulting in uniform amplification (see section 7). There must be found a compromise between the demand and the limits given by the electronics. The high voltage is limited by the supply unit (nominally 2500 V) and the linearity of the PMT-s. The CFD threshold is not recommended to set lower than 4×5.5 mV. For pulse shape discrimination the fast component must fulfill also the above discrimination requirements. The time range determines the lower limit of the dynamic range as well. The 0.5–1 MeVee requirement can be fulfilled (see fig. 26c) and it is not recommended to use the

side information for analysis because it arises complicated problems making the results questionable requiring Monte Carlo analysis.

For the n/γ discrimination one must use also the position corrected geometric mean of the fast components and of the total charges.

5. NEUTRON EFFICIENCY

For the reconstruction of the neutron energy distribution one needs the neutron detection efficiency. One has to know event by event that one detected particle represents how many particles directed into the solid angle spanned by the detector. In case of neutral particles the efficiency involves a charged particle producing conversion process and the detection of a charged particle. The position of the interacton is not known therefore one can estimate only an average probability of the detection. The efficiency is estimated by computer codes calculating the light production from the cross section data of the interactions and the geometry. Such codes were applied for the CAN neutron detectors in the earlier experiments. For a neutron of given energy the detection efficiency is calculated as a function of the discrimination level. In case of the cells the efficiency has to be expessed as a function of the software discrimination level in the position corrected geometric mean of the total charges corresponding to the energy deposit. The considerations and measurements below are very instructive but probably they do not substitute a Monte Carlo simulation for the geometry of the cell which can be taken infinite in one direction.

In principle one can define equivalent sections in the cell which can be compared to the CAN detector. The thicknesses of the detectors are almost equal so the equivalent section can be defined having the same volume as the CAN detector. In event by even analysis the virtual equivalent detector

— in principle — can be cut so that the event should be in the middle of the section therefore we do not expect any effect of the position (x) of the interaction. However, some differences have to be considered whether they have remarkable effect especially in the quantitative comparision.

While the CAN detector has a real surface on every side, the cell section has virtual surfaces perpendicular to the axis and the cell has upper and lower neighbours. One can estimate the effect of the surface escape. The escaping electrons near the surface of the detector produce less signal reducing the Compton "peak", the efficiency, giving a low energy contribution. Because of the surface one has to reduce the sensitive volume of the detector. The missing volume can be approximated by the escape surface area $\times$ skin thickness s. The surface corrected volumes of the CAN and cell sections:

$$V_{can} = r^2\pi w_1 - 2(r\pi w_1 + r^2\pi)s$$

$$V_{cell} = \Delta x h w_2 - 2\Delta x(h + w_2)s,$$

where r is the radius and w_1 the width of the CAN detector, while Δx is the length, h the height, w_2 the width of the elementary detector section. The nominal inner size of the height and thickness of the cell are 7.7 and 6.4 cm, respectively, while the CAN has a diameter of 5" and thickness 3". The equivalent sections have 19.6 cm front size. The range of the 4 MeV electron in NE213 scintillator is $R = 20$ mm. The skin width is the distance averaged by the solid angle between 0 and R, for electrons $s = \frac{3}{8}R = 0.75$ cm. This overestimates the effect while the measure of the energy loss was not taken into account. Probably the range can be reduced by a factor < 1 which corresponds to a remarkable energy loss. The proton range is about 0.25 mm therefore for neutrons the surface loss can be neglected. The escape volumes for electrons are rather large (418 and 414 cm^3 from the 965 cm^3 volume for the CAN and the equivalent cell sections, respectively, using $s = 0.75$ cm),

but they accidentally are fairly equal and their effect can be neglected in the comparison, therefore one can expect that the neutron and the γ ratio as well should measure the solid angle difference. The ratios of the escape surface to the volume are almost equal:

$$\frac{F}{V}|_{can} = 2\frac{r+w_1}{rw_1} = 0.5774$$

$$\frac{F}{V}|_{cell} = 2\frac{h+w_2}{hw_2} = 0.5722.$$

Please notice that the cell ratio is independent on the length of the section Therefore we expect that the neutron detection efficiency is with high accuracy equal to the efficiency calculated for the CAN detector.

The effect of the cross scattering from the next cells and from outside of the virtual surface can be a few percent in the low energy (low charge) part of the spectrum. The effect of the inscattering through the virtual surface (in the quantitative comparision) is probably even less for the primary light produced (outside) will dominate and the event will fall out of the section measured. Anyway we do not expect less efficiency than of the CAN but even a little bit larger.

In order to check the efficiency the cell was compared to a CAN detector. We took CELL 2 in individual neutron single mode and the CAN 21 was put into the channel of PMT 3. The anode signal of the CAN PMT (at -1700 V) was splitted into 2 ways. One of the signals was inverted by a pulse transformer for the dynode patch panel. The n/γ separation line was fitted as mentioned in section 4. The ^{60}Co, ThC", and PuBe γ-ray energy calibration of the middle section ($\pm$10 cm) of the cell (*sqtt*) and of the CAN (*qtot*) is shown in fig 16. The CAN is remarkably nonlinear.

The PuBe neutron source was placed at a distance $l = 161.1$ cm in front of the middle of the cell and the CAN was at 168.5 cm aside. By position cuts equivalent detectors were defined having the same volume.

The PuBe γ energy spectra are shown in fig. 17 measured by the CAN and the equivalent cell sections at $x = \pm 9.8$ cm and $x = \pm(80 \pm 9.8)$ cm. The shape of the γ spectra is similar. The yield of the middle and far sections corresponds to the solid angle change. The counting rate is in a section at angle α

$$N = N_0 \frac{h\Delta x \cos\alpha}{4\pi(l^2 + x^2)} \frac{w}{\cos\alpha} \eta_0,$$

where η_0 is the reduced efficiency for unit width at a given discrimination level and energy composition (PuBe source). Here we used the approximation that $N = \chi(E) N_0 d\Omega (1 - e^{\frac{w'}{\lambda}}) \approx \chi(E) N_0 d\Omega \frac{w'}{\lambda}$; $\frac{\chi(E)}{\lambda} = \eta_0$. Let us notice that the counting rate is proportional to the detector volume V

$$N = N_0 \frac{V}{4\pi d^2} \eta_0,$$

and d is the source detector distance. The ratio of the far and middle sections is $\frac{N_{far}}{N_{mid}} = \frac{l^2}{l^2 + x^2} = 0.80$. The shape of the CAN γ spectrum is similar, however, it is also about 80% of the middle equivalent cell section. The neutron spectra are compared in fig. 18. The shape of the CAN neutron spectrum differs from the cell spectra, it seems to be expanded. For comparison the relative spectra normalized to the middle section are also displayed. In fig. 19 the averaged γ and neutron spectra are plotted of the far sections. The neutron ratios are constant between 1–4 MeVee corresponding to the solid angle change (0.80), while the γ ratios are somewhat larger especially at small energies because of the relative larger cosmics contribution far from the source.

The ratios for the CAN detector are shown in fig. 20. The γ ratios near the Compton "peak" are constant about 0.80 which is significantly less than expected from the solid angle. The data taking happened simultainously at the same real time therefore the dead time must be equal. To solve the contradiction we analysed the cell spectra. In fig. 21 there are plotted the relative efficiencies of the neutron and γ-ray of 10 cm long elementary detector

sections — taken between 1 and 4 MeVee, and normalized to the middle of the cell — as a function of the position. The solid line represents the the solid angle dependence corresponding to a source–cell distance $l = 161.1$ cm as given upper. The data fit better to the dashed line calculated with $l = 126$ cm. We are afraid that we made a mistake in the measuring or recording the source distance. As a check in fig. 22 we show the similar position dependence plots measured with PuBe source put onto the ladder in the middle of the platform before the front wall at about 50 cm from the cell. The intensity ratio of the central sections of the second and first wall (cells 8 and 23-25, respectively) is 0.23 which corresponds to the estimated distances: 50 and 104 cm. The fits using these distances are acceptable regarding that the source is very close to the first wall. Accepting the modified source distance the CAN detector has to be compared rather to the far sections and the agreement is fairly good. The larger width of the γ position distribution is the result of the relative larger contribution of the cosmics background and the deviation from the simple geometric function far from the middle probably can be attributed to the larger role of the cross scattering with the growing entrance angle.

In order to check the effect of the virtual surface of the section we compared the relative efficiencies measured with different section volumes. In fig. 23 there are plotted the detector yields between 1 and 4 MeVee of a series of symmetric sections around $x = 0$ with ± 2 cm steps normalized to the ± 10 cm detector. The plot reveals a linear function on the detector length upto quite long sections showing that the virtual surface has no decisive role. The curves show the averaged solid angle functions calculated for two source distances.

The energy dependence of the neutron ratio, the expanded neutron spectrum is connected probably to the fact that the strong nonlinearity got for the electrons is not valid for protons. In the space charge nonlinearity the

fast component of the scintillation is dominant. The response, the calibration function of the PMT is similar for protons and electrons but a given nonlinearity corresponds to somewhat larger total charge for protons than electrons because of the larger slow component. The energy calibration can be written superimposed the linear slow and nonlinear fast components:

$$E = c_0 + c1(Q_{fast} + Q_{slow}) + c_2 Q_{fast}^2.$$

The fast component is proportional to the total charge (factor χ):

$$E = c_0 + c_1 Q_{tot} + c_2 (Q_{tot}\chi)^2.$$

From this interpretation it is clear that for the nonlinear CAN the calibration function depends on the contribution of the fast component. The ratio of the fast components can be estimated from the spectra of the fast component ($sqft$) gated by narrow total charge window as shown in fig. 7. Using the ratio of the γ and n fast components κ we can approximate the energy calibration for protons from the γ calibration constants for the CAN:

$$Epeq = c_0 + c_1 cqtt + c_2 \left(\frac{cqtt}{\kappa}\right)^2.$$

The calibration and the ratios are plotted in figs 16, 20 and 24. With $\kappa = 1.16$ taken from the data of fig. 7 in the nonlinear region the 4 MeVee neutron ratio agrees with the γ ratio (fig. 20). At lower energies the ratio decreases probably because of the neutrons scattered from the neighbouring cells and through the virtual surfaces increase the divisor. Supposedly the same cross scattering reduces the γ ratios at lower energies overcompensating the larger cosmics contribution.

The earlier neutron efficiency studies [2] compared the cell 32 (second wall 7^{th} cell) and the CAN 24 at -1800 V. The comparison with our results is rather difficult. The CAN detector was rather linear but the measurements

were performed alternativly and as the volume of the cell is approximately 10 times larger than the CAN they had to be normalized by the measured live time. We agree on that the CAN and cell spectra are similar, their ratio is energy independent and doesn't depend on the position above a certain discrimination level. The ratio of the neutron efficiency, however, was found larger than the γ one but it is hard to compare to our results for it depends strongly on the discrimination level. On the contrary of our present results the cell efficiency was about 70% of the CAN which can be the consequence of the dead time calculation.

In summary we can say that the results got by the cell are consistent for the γ and neutron detection. The neutron spectra measures the solid angle, the γ spectra have some cosmics background contribution, and the cosmics background spectra are equal. The comparison with the CAN detector — although was not performed with proper care — we think that it probably verifies the idea that the efficiency of the cell agrees with an equivalent section of the cell and probably can be calculated by the codes used for the CAN detectors. The threshold has to be determined in the energy value calculated from the position corrected geometric mean of the left and right charges. The measused energy dependence of the neutron spectrum can be explained by the hypothesis that the strong nonlinearity of the γ energy calibration for the CAN detector is not valid for protons. The nonlinearity for the neutrons in the CAN detector has to be reduced by a transformation factor estimated from the ratio of the fast components. From the comparison one can suppose that the low energy part of the neutron and γ spectra in the cell are enhanced by cross scattering from the next cells.

We suggest that the efficiency calculations can be used for the position corrected geometric mean energy discrimination but in the reconstruction of the neutron energy distribution one has to take into account the cross

scattering, the coincidences between the neighbouring cells.

6. PULSE SHAPE DISCRIMINATION

In special liquid scintillators the light emission has two well distinguishable components and the quenching of the fast one remarkably depends on the specific ionization of the detected particles. With these scintillators one can separate the γ (electron) and neutron (proton) events analysing the pulse shape of the scintillations.

The simplest way to analyse the pulse shape was reported by Heltsley at al. [3]. With apropriate delays one can measure the total charge and the tail charge in every scintillation by a QDC and from the comparison of the two charges it can be decided whether the particle was neutron or γ-ray. In the n-WALL the scintillations are detected on both ends of the cells having about 0 ± 12 ns time differences and in one event several cells can fire therefore the above method cannot be used in reasonable money and electronics limits. The problem is that the charges to be measured must be synchronized to the QDC gate. In case of several PMT-s fireing one has to use individual gates for every channel or to apply some asynchron method.

J. Tőke pulished a PSD circuit [4] producing a head charge pulse differentiating and cutting the positive part of the inverted pulse. This head charge pulse already can be measured asynchronously with a common gate. The circuit is built of 2 transistors and needs individual setting of the cut level. We applied a more simple method submitted for US patent [5].

Our asynchron pulse shape discrimination circuit applies the cable clipping method. It uses that the reflected positive charge from a short cut cable will compensate the tail charge producing a pulse representing the fast component. The clipping cable has to be separated activly from the anode circuit therefore

an emitter follower is implemented between the anode splitter and clipping cable. This solution is very simple, stable, doesn't need any adjustment, and even its particle resolution, the PSD figure of merit is more than 90% of the reference synchron method. In figs 25-26 is demonstrated the power of our asynchronous PSD cicuit. In the function of the energy there are plotted the PSD figure, the FOM of the discrimination, and the energy spectra. Further advantage of the cable clipping PSD is that it has a high impedance input and do not scale down the anode pulse (*Qtot*) and it measures and compares the fast component to the total one therefore it has rather linear separation line even if the PMT is not linear. (The XP4312B PMT-s of the n-WALL are fairly linear.)

Notwithstanding that the PSD circuits are working their working principle is not quite understood. In principle integrating long time enough the charge and the cable reflected charge the net charge ought to be zero. Probably the input circuit of the QDC plays important role. With FERA e.g. the circuit is not working the FERA feels really zero net charge below a certain rather high threshold.

The emitter follower has a low impedance output therefore if the input of the cable is not terminated by a serial resistor the reflected signal is reflected from the emitter follower too resulting in an oscillating positive tail. In spite of the oscillations this solution seems to be the optimal for the termination drops the signal to the half elevating the discrimination level.

The dynode pulse is used for the timing and charge measuring gate. The 12^{th} (last) dynode is connected to the dynode patch panel which mathces the 50 Ω input and 100 Ω output circuits, reduces the signal by 12 dB, and inverts the signal by a pulse transformer. The anode signals are delayed by 100 ns and connected to the anode patch panel which integrates the PSD circuits too. There is a 2-way splitter *i)* for the total charge and the emitter follower

for the fast component and *ii)* the 12 dB attenuated total charge and emitter follower for the attenuated fast component. The delay cables are 8 and 12 ns for the nonattenuated and the attenuated signals, respectively.

After the reconstruction of the NSCL accelerators the electronics committee wants to replace the obsolate LeCroy QDC-s with some other more modern, faster units. Therefore we tested some other cuircuits. The density differences of the inputs of the LeCroy FERA, or the Phillips 7167 and LeCroy 2249W QDC-s is not significant (16 versus 12 channels). But the 2249W QDC is really very slow. Its conversion time is about 80 μs while the Phillips QDC has about 7.2 μs, however, the units are not equivalent in the PSD threshold and resolution. In the following we compare some PSD possibilities.

Testing the different QDC units we substituted the LeCroy 2249W QDC in BANK 1 with several Phillips 7167 QDC-s and LeCroy 4300 FERA units measuring the fast components. Therefore the performance of the left side data processing has to be compared. The hardware threshold was set to 6×5.5 mV. In order to estimate the PSD threshold energy from the side spectrum let us notice that the geometric mean is equal with the signal from the middle of the cell — in symmetric *qtot* setup. Let us remember that the middle value is about 1.55 times the far one (see fig 8). The geometric mean spectra of the PuBe γ-ray (4.439 MeV) are plotted in fig. 12 measured with the standard data taking. From the middle value (700 channel) of ht *sqtt* spectrum one can estimate that the *qtot* far end value of a 4 MeVee particle is about in the 450^{th} channel, i.e. 1 MeVee corresponds to 113 channels in *qtot*. The standard circuit with the nonterminated emitter follower and the LeCroy 2249W QDC gives the scatter plot shown in fig 27. The hardware threshold of the PSD is around $qtot = 60$ channels corresponding to 0.5 MeVee. The nonterminated emitter follower is a non elegant solution with the oscillating pulse therefore we tested the emitter follower terminated by a serial 47 Ω

resistor too. We didn't expect improvement because the serial resistor divides the signal and elevates the threshold anyway we checked and the result is shown in fig. 28. The slope decreased by a factor 2.2 and the threshold went up to about 1.5 MeVee. The Phillips 7167 QDC (12 bits) was pluged in into the slot of the LeCroy 2249 QDC. Figure 29 shows the scatter plot measured. The slope agrees with the reference one but the threshold moved to about 1.2 MeVee. This unit can be used if the hardware threshold acceptable for the experiment. We tested the LeCroy 4300 FERA too for the measurement of the fast component. The slope is the same as the standard method but the threshold is about 7.5 MeVee see fig. 30. The FERA measures zero net charge untill the positive clipping diode at the input begins to cut the positive part of the input pulse. Above this value the net charge grows as in the standard case.

From the above comparison we can say that the standard solution is the best. It is simple, stable, and very cheap. Anyway if one makes compromise with a higher energy limit about 1.5–2 MeVee can use e.g. the Phillips 7167 QDC. In fig. 31 the FOM of the standard (LeCroy 2249W) and the Phillips 7167 ADC are compared. They differ only in the low energy part. However, using the Phillips ADC probably one has to change the PSD patch panel too because the units need different cabling.

We recommend to update the dynode patch panel too. It matches the 50 Ω input but doesn't match to the 100 Ω output. This change is a little simplification, doesn't touch the construction.

7. HARDWARE SETTING

For the hardware setting of the n-WALL electronics one must decide the dynamic range of the neutron energies to be measured. In the decision one

must find a compromise between the requirements and the limitations of the detector and the electonic units. There are limitations in the time and charge measurements. Because of the light attenuation the hardware charge discrimination has to be set about one and a half times lower than the actual software threshold, for as was mentioned in section 4 the geometric mean is equal to the middle value — in symmetric setting — and the far value is about 67% of the middle one. The charge threshold determines the efficiency of the detection while the time limit excludes the events outside the time window.

The charge threshold is determined by the CFD discrimination level. Turning on the CAMAC crate the LeCroy 3420 CFD has to be initialized. The discrimination level, the output pulse width, and the dead time has to be set. The pulse width was set to minimum 25 ns, the dead time which inhibits the multiple fireing of the channels was set to maximum 250 ns (CAMAC command F(17)A(1) 15). The threshold can be set between 0 and -1 V in 5.5 mV steps with the CAMAC command F(16)A(i). It is not recommended to set less than 4×5.5 mV. At the nominal HV settings the energy threshold in the position corrected geometric mean is plotted in fig. 32 as a function of the discrimination. With 6×5.5 mV about 0.5 MeVee charge threshold can be reached for neutrons (see fig. 26c), although one has to keep in mind that the cross talk depends on the CFD discrimination level.

The time window is determined by the TFC output amplitude and by the coincidence and dead time gates. The high energy limit of the dynamic range is determined by the time resolution of the detector and the length of the path of flight. For the time resolution FWHM $\approx$ 1 ns reasonable choice is $dt = 200$ ps which ensures in 1500 channels 300 ns TOF range to measure. At 5 m path of flight it corresponds to 1.5 MeV low energy limit (see fig. 33). The $dt = 200$ ps channel width has to be set adjusting the output current of the TFC. The channel width of the LeCroy FERA 4300B is 0.25 pC and the

saturation is at 480 pC which corresponds to 1920 channels. From this

$$i \cdot dt \cdot 1920 = 480 \ , \quad \text{and the output amplitude} \quad U = i \cdot 48 = \frac{12}{dt} \ \text{V}$$

on 48 Ω load resistance. In fig. 33 there is plotted the function of the channel width and TFC setting. The output amplitude has to be set to 60 mV for $dt = 200$ ps.

The input of the TFC in common stop mode is always open therefore the start pulses have to be gated for the dead time. The TFC dead time generator is shorter than the coincidence gate (the dynamic range) therefore we use the CFD NIM veto input for the live time definition. The dead time is made from the leader PMT pulse after the dynamic range, by the computer busy signal, and for the FERA and QDC recovery time (minimum 2 μs) after a fast clear.

The delay of the CFD was set to 10 ns (delay chip 1505-50B). The summed NIM pulse was used for NIM fast logic units producing the charge measuring gates (dynamic range + 300 ns) and coincidence trigger. The summed ECL pulse gave the TFC start (STRT) triggering the gate pulse for the time FERA. The gate must slightly longer than the longest analogue output generating an overflow in the FERA which will be suppressed and not read out in the measurement. The gate was set to 470 ns. The CFD outputs must be delayed that the TFC output should sit inside the gate at the input of the FERA at least by 20 ns. We used 20 units ribbon cable corresponding 55 ns delay (1 unit is 51.88 cm, 2.8 ns). For BANK 4 the cable was 18 units long, probably that caused the degradation of the time resolution of BANK 4!

The analogue charge measuring QDC and FERA gates must preceed the leading pulses **at least 20 ns.** This is very important! Don't forget that the NIM-ECL converter has also about 10 ns delay! (This has been missed in the beginning of the experiment.) Important warning is that the FERA input delay has to be checked directly, on the inputs and one must not make

a compromise! Less delay makes the conversion unstable smearing the time resolution — in worse cases depending on the pulse height — and washes the PSD mixing the neutron and γ events (like a fan).

The nitrogen UV laser has a main distributor branching the light into four main branches with 5 m double quartz fibers. One is used for the reference detector, two are connected to the distributors at the side wall of the n-WALL, and there is a spare one. The wall distributors have 32 outputs each with 3 m fibers for the cells. In the geometric middle of the cells there is a screw glued for the connection of the fibers. The fibers are polished but the distributors have no any optical contact but even there are spaces for attenuators. The thermocopy foils are used for attenuation. The attenuation of the foils are 0.1, 0.42, and 0.73 for the red, blue, and clear foils, respectively. The laser light is fanned fairly uniformly and with an attenuator about 50 the laser pulse corresponds to 5 MeVee.

The dynode fast timing CAMAC crate and the charge measuring crates must be a powerfull high current ones for ± 6 V. The power consumptions are: CFD +6V 1A, −6V 1.75A, TFC −6V 1.5A, FERA +6V 2.1A −6V 2.7A. For 32 cells all together the timing CAMAC crate needs +21.8 A and −24.2 A, while the analogue crate +30.0 A and −20.5 A.

8. SOFTWARE TOOLS

Because of the large number of the PMT-s and cells some computer programs were developed which work on a series of spectra automatically evaluating them supporting the on- and offline calibration and parameter setting. The programs read spectra in LMD format but can be applied for SARA or HBOOK/ZEBRA format for program PAW too.

PEAK_fit.exe program performs a peak search with cross correlation

method using a Gaussian filter function and fits a Gaussian curve to the peaks found producing a table of the fit results. The code can be used for the pedestal and laser peak evaluations.

CMPT_edge.exe program searches the Compton edge in γ spectra with cross correlation method and writes into a table. The program expects a series of γ spectra of ^{60}Co, ThC", and PuBe sources with a position window in the middle of the cell.

nWALL_E_cal.exe program calculates the energy calibration function of the PMT-s using the pedestal and γ-ray tables produced by PEAK_fit and CMPT_edge codes. As an option the program can offer a new HV setting resulting in a given amplification. The fine tuning of the HV results in a uniform, symmetric setting of the PMT-s which is advantegous for the analysis and the optimal exploitation of the hardware limits. The program uses the HV characteristics of the Philips PMT XP4312B (see data sheet Philips Photonics Mar-94)

$$Q = Q_0 e^{\frac{\Delta V}{\lambda}}$$

with $\lambda = 267$ one get

$$\Delta V = 267 \cdot \ln \frac{Q_0}{Q}.$$

The programs reads the HV_old.usr table and produces a HV_new.usr file. We used to set 0.005 MeV/channel amplification.

n_GAMMA_cut.exe program fits two Gaussian fuctions to the *sqfst* spectra gated on some narrow windows in *sqtot* fitting a 2^{nd} order polynomial separation line through the valleys for online n/γ discrimination.

HV_nWALL.exe program turns the HV on to the PMT-s of a cell for a given time pair wisely in cycle used for the individual biasing in the laser synchronization runs. The calibration can be accelerated biasing the cells modulo 16 symultainously using separate CAMAC units.

9. SUMMARY

Calibration mesurements were made with the setup of the n-WALL used in experiment NSCL #98016. We determined new, better pedestal values and performed the time calibration with laser synchronization by individual HV biasing the cells. A new time calibration method is elaborated and used based on measured values like the laser peak time T_{0i}, channel width dt_i, and the effective velocity of the light v_{eff} in the cell. Using the laser synchronization the measured channel widths can be corrected with high accuracy and there is only one delay which has to be determined from the promt γ peak for the absolute time calibration. All the time spectra can be summed into one time spectrum and there is a hope that in the sum spectrum one can locate a tiny promt γ-ray peak.

The position dependence of the light collection is analysed. The light attenuation depends on the extinction in the liquid, on the reflection loss in the total reflection on the outer surface of the glass tube, and on the solid angle. The attenuation is not simple exponential function of the distance therefore the geometric mean of the charges measured at the two ends is slightly position dependent. We suggest a position correction of the geometric mean which improves the energy resolution of the charge measurement.

We tried to check the neutron efficiency of the cells comparing to a CAN detector used in earlier experiments. The neutron and γ-ray spectra of the elementary sections of the cell are consistent, i.e. the neutron yield corresponds to the solid angle difference and the γ yield is relatively larger in the section further away from the source because of the uniform cosmics background. However, unfortunatly during the offline analysis it turned out that the comparison was not performed with proper care and the results cannot be used for quantitative comparison. The CAN γ spectrum is similar but

was measured to be smaller supposedly because of an error of the distance measurement. The comparison of the neutron spectrum is even less successful because of the strong nonlinearity of the CAN detector. But even we suggest that the codes calculating the neutron efficiency can be used for the cells but the cross scattering from the next cells, the coincidences have to be taken into account. We must appreciate that the choice of the XP4312B PMT-s was a good one for they are fairly linear and fit to the cell size.

The cross talk in the timing circuit is a serious problem. We found that probably the LeCroy 3420 CFD is responsible for the cross talk they ought to be changed in the new applications. The KFKI has a CFD [6] used in the NA49 CERN experiment for 400 channels having no cross talk problem. The KFKI CFD is built in VME standard 16 channels per unit but it can be built into CAMAC system too. I shall investigate the cross talk of the unit in the near future.

The change of the obsolate LeCroy 2249W QDC is questionable. May be it could be saved for alternative usage. One must accept a compromise whether the lower energy threshold, or the speed of data taking is more important. With the LeCroy 2249W QDC one can have about 0.5 MeVee threshold for neutron detection while with the Phillips 7167 QDC only 1.2 MeVee. As an option one can search for an other QDC or PSD circuit too. Anyway the change of the QDC measuring the fast components may mean the reconstruction of the PSD patch panel too because of the different cabling. We suggest that he dynode patch panel should be updated too.

I am to study the PSD circuit in order to understand its working principle and to clarify the role of the QDC input circuits. And I want to make a detailed documentation of the electronics setup.

APPENDIX I.

List of the parameters [1] and algorithms used in the paper.

Measured parameters: $i = 1, 2, ..., 64$

$Time(i)$	PMT time [ch]
$Qtot(i)$	total charge [ch]
$Qfst(i)$	fast charge component [ch]

Pseudo PMT parameters:

$time(i) = 5(Time(i) + \delta - T_0(i)) \cdot dt(i)$	time [200 ps]
$qtot(i) = Qtot(i) - Ptot(i)$	pedestal corr. total charge
$qfst(i) = Qfst(i) - Pfst(i)$	pedestal corr. fast comp.

Pseudo CELL parameters: $k = 1, 2, ..., 32$

$sqtt(k) = \sqrt{(qtot_L(k) + \delta_1) \cdot (qtot_R(k) + \delta_2)}$	total geom. mean
$sqft(k) = \sqrt{(qfst_L(k) + \delta_1) \cdot (qfst_R(k) + \delta_2)}$	fast comp. geom. mean
$posn(k) = (time_R(k) - time_L(k))/5 \cdot v_{eff}$	position [cm]
$tavg(k) = (time_L(k) + time_R(k))/2$	average time [200 ps]
$ngCL(k) = sqft(k) - (v_0(k) + v_1(k)sqtt(k) + v_2(k)sqtt(k)^2)$	PSD [neutron < 0]
$cqtt(k) = sqtt(k)(1 - x_1posn(k)^2)$	pos. corr. total charge
$cqft(k) = sqft(k)(1 - x_2posn(k)^2)$	pos. corr. fast comp.
$Eeeq(k) = c_0(k) + c_1(k)cqtt(k) + c_2(k)cqtt(k)^2$	energy [MeVee]

Parameters (MSU.LEX, see Appendix II.):

$Ptot(i)$	Qtot pedestal
$Pfst(i)$	Qfst pedestal
$T_0(i)$	laser time peak [ch]
$dt(i)$	time channel width [ns]
$v_0(k), v_1(k), v_2(k)$	separation line params

[1] Not respecting the attenuated charges

$c_0(k), c_1(k), c_2(k)$	energy calibration params
x_1, x_2	pos. corr. params (total, fast)
$v_{eff} = 7.83$	eff. light velocity [cm/ns]
δ	$0 \leq \delta < 1$ random number

APPENDIX II.

In the experiment NSCL #98016 the active cells were 5–20 and 37–52 corresponding to logical cell numbers 1–16 and 17–32. Bank 1 contains PMT 1–16 (cell 1–16 left), bank 2 PMT 17–32 (cell 1–16 right), bank 3 PMT 33–48 (cell 17–32 left), and bank 4 PMT 49–64 (cell 17–32 right).

The HV table follows the hardware sequence left–right PMTs of cell 1,2,3, etc, the not used PMT-s are flagged by negative sequence number.

```
Qtot pedestals Ptot:
 73  51  92  60  66  67  53  78
 69  71  66  68  87  66  58  74
 31   8  11   3  16   6  27   3
  9   6  14  16  11   6   5   7
 37  50  61  45  39  21  43  23
 48  37  43  52  34  36  42  30
 18  21  23  45  41  35  36  26
 22  40  25  22  40  32  32  26
Qfst pedestals Pfst:
 14  23  14  12  26  24  18  26
 28  24  21  23   7   1   1   1
 21  19  15  20  23  20  22  32
 29  24  23  26   4   1   8  37
  6  24  31  23  25  19  33  51
 42  44  39  42  35  16  19  22
 20  17  13  17  23  16  22  25
 27  28  20  27  18  14  18  10
Qatt pedestals Patt:
 17  16  19  13  14  17  20  16
 20  18  18  14  18  22  12  12
 23  17  32   6   6   7  18  13
```

```
 16  13   0  21   8  18  10   0
 12   3  18   4   4   7  11   1
  0   2   7   7  20   5  12   5
  0   0   6   2   0   0   0   0
  2   2   9   0   1   0   0   0
Qaft pedestals Paft:
 14  12   3   7  16   5   1   9
 23  15  17  20   9  15  13   6
 19  15  20  12  20  19  22  28
 30  22  25  24  15  10  18  21
214 157  10   3  10  10  14  17
 13  16  17  17  20  18  20  11
 27  26  21  19  20  28   1  31
 30  27  33  34  15  12  18  26
Laser peak positions P0:
1004.0  979.9  989.2  979.9  987.8  985.8  991.1  989.0
 986.0 1000.0  998.2  978.9  991.8  987.8  981.3  997.0
 994.7  986.6  993.9  977.5 1000.0  993.7  994.1  994.0
1007.0  990.1 1004.0  978.6  995.5  988.2  998.5  986.8
 976.5  977.5  978.9  976.1  984.2  965.5  964.1  978.2
 972.0  967.5  982.8  976.7  970.3  979.9  979.0  987.5
1022.0  999.4 1018.0 1004.0 1019.0  997.2 1025.0 1006.0
1011.0 1008.0 1019.0 1002.0  997.3 1027.0 1002.0 1019.0
Time calibration dt:
 0.2087  0.2099  0.2090  0.2096  0.2110  0.2093  0.2093  0.2100
 0.2098  0.2085  0.2099  0.2097  0.2099  0.2098  0.2112  0.2085
 0.2130  0.2121  0.2105  0.2120  0.2101  0.2091  0.2119  0.2108
 0.2106  0.2110  0.2109  0.2137  0.2088  0.2120  0.2103  0.2114
 0.2114  0.2098  0.2102  0.2103  0.2098  0.2115  0.2107  0.2104
 0.2110  0.2120  0.2096  0.2100  0.2093  0.2104  0.2099  0.2085
 0.2085  0.2099  0.2074  0.2092  0.2088  0.2122  0.2073  0.2104
 0.2089  0.2080  0.2094  0.2089  0.2101  0.2071  0.2104  0.2071
Energy calibration c0, c1, c2:
-.1611e-1 -.2582e-1 -.2802e-1 -.8158e-2 -.6860e-2 -.8773e-3 -.2582e-1  .8249e-2
-.9281e-2 -.8773e-3 -.8773e-3 -.5516e-2 -.7984e-2  .8526e-2 -.1014e-1 -.1284e-1
-.6315e-2 -.1485e-1 -.9348e-2  .2020e-2 -.1141e-2  .2285e-2 -.6618e-2 -.2080e-2
 .7541e-2  .3831e-2 -.5502e-2  .2149e-2  .2020e-2 -.5462e-2 -.8158e-2 -.1592e-1
 .6298e-2  .6370e-2  .6452e-2  .6311e-2  .6262e-2  .6367e-2  .6370e-2  .6849e-2
 .5802e-2  .6367e-2  .6367e-2  .6211e-2  .5594e-2  .5943e-2  .5677e-2  .6101e-2
 .5921e-2  .6250e-2  .6039e-2  .6119e-2  .6244e-2  .6542e-2  .6318e-2  .7521e-2
 .6049e-2  .6255e-2  .5839e-2  .6603e-2  .6119e-2  .7483e-2  .6311e-2  .7002e-2
-.1944e-6 -.4540e-6 -.6779e-6 -.1723e-6 -.3723e-6 -.2770e-6 -.4540e-6 -.6233e-6
-.4171e-7 -.2770e-6 -.2770e-6  .1036e-6  .1314e-6  .5721e-7 -.7594e-7 -.4424e-6
 .8543e-6 -.6248e-7  .5231e-6  .8624e-6  .5018e-6  .7534e-6  .7609e-6  .4866e-6
 .6089e-6  .1018e-5  .2467e-6  .1868e-5  .8424e-6  .5726e-6 -.1723e-6  .4832e-6
```

```
n/gamma  separation line v0, v1, v2:
 -23.6  -23.7  -24.6  -29.9  -29.7  -29.7  -29.2  -24.6
 -31.4  -20.0  -29.6  -25.2  -30.9  -21.1  -28.1  -34.4
 -22.7  -21.7  -25.7  -28.9  -27.9  -18.3  -33.8  -27.2
 -32.1  -26.1  -29.8  -21.2  -30.0  -27.0  -26.6  -24.5
 .5184  .5079  .5219  .5303  .5381  .5300  .5300  .5098
 .5465  .5100  .5509  .4741  .5368  .5093  .5525  .5506
 .5547  .5021  .5252  .5066  .5076  .5093  .5253  .5068
 .5612  .5166  .5495  .4777  .5345  .5434  .5124  .4930
 .7793e-4 .4405e-4 .5598e-4 .2660e-4 .4510e-4 .1593e-4 .3430e-4 .5396e-4
 .1711e-4 .4360e-4 .2595e-4 .6616e-4 .1937e-4 .4647e-4 .1592e-5 .1527e-4
 .2496e-4 .7593e-4 .5301e-4 .2853e-4 .4259e-4 .7918e-4 .1281e-4 .8021e-4
 .1647e-4 .4740e-4 .2873e-4 .1103e-3 .9569e-5 .9832e-5 .5204e-4 .0499e-4
Eeeq position correction x1, x2:
.17449e-4  .22682e-4
```

APPENDIX III.

Starting procedure of the n-WALL. Operation modes. Hardware, software actions. Suggested set of spectra.

1. Initialize CFD.
   SW: Set thresholds: F(16)A(0) 4
   Set width and dead time: F(17)A(1) 15
   25 ns 250 ns
   Set mask register: F(17)A(0)

2. Set TFC
   HW: Set gate width 470 ns
   non stopped OVF
   Set output amplitude 61 mV
   dt=200 ps

3. Measure t-FERA pedestals.
   Mode: neutron single
   Source: cosmics
   SW: Set Time pedestals to 0 (Prepare CAMAC command block)
   HW: Disconnect TFC input cable.
   Spectra: Time(i) ; i=1 - 64
   Analyse: Pedestal values Ptim(i) (PEAK_fit)
   Take Ptim > largest pedestal channel in order to reject false trigger
   But too large pedestal cuts the useful dynamic range.

4. Preliminary time calibration I.

Mode: Laser coincidence
Source: Simultainous laser pulse
SW: Set time pedestals Ptim(i) with CAMAC command
for automatic pedestal subtraction
HW: Shift the laser peak to about 1000 channel with the reference STOP delay
Spectra: Time(i) ; i=1 - 64
Analyse: laser peak positions T0(i) (PEAK_fit) for preliminary time calibration

5. Preliminary time calibration II. (Continuation of step 4.)
HW: Delay laser reference stop by 10 n
Spectra: Time(i) ; i=1 - 64
Analyse: laser peak positions for dt (PEAK_fit)

6. Measure QDC and charge FERA pedestals
Mode: neutron single
Source: Cosmics
HW: Swap the first and second wall ribbon cables at the CFD inputs
Spectra: Qtot(i), Qfst(i), Qatt(i), Qaft(i) ; i=1 - 64
Analyse: the pedestals (PEAK_fit)

7. Preliminary energy calibration.
Mode: neutron single
Source: 60-Co, ThC" and PuBe between the WALLs
Spectra: qtot(i) & [-10<=posn(k)<+10] ; i=1 - 64 (with +-10 cm position cut)
Analyse: Compton edges (CMPT_edge)

8. Calculate energy calibration and produce a new HV table
for 5 keV/channel amplification.
SW: run nWALL_Ecal

9. Change HV

10. Time calibration I. Channel width calibration.
Mode: Laser coincidence
Source: simultanous laser pulses
HW: Change the stop delay in 10 ns steps.
Use the NIM cable delay unit pluging the 10 ns inputs instead of 20 ns
(the connecting cables not changed)
Spectra: time(i) ; i=1 - 64
Analyse: the spectra and get the final channel width.

11. Time calibration II. Laser synchronization.
Mode: Laser coincidence + 10% n-single
Source: Laser with individual biasing + cosmics background

SW: Use HV_nWALL program for individual biasing with automatic stepping.
10 minuits measuring time took 11 hour measuring time!
Spectra: time(i), qtot(i) ; i= 1 - 64
Analyse: Laser time spectra T0 (PEAK_fit). Note that the calibration can be accelerated by measuring the separated banks simultainously.

12. Energy calibration.
Repeat step 7. (The energy calibration can be performed after the experiment because the HV changes are usually small.)
Spectra: sqtt(k),qtot(i) ; k=1 - 32, i=1 - 64
sqat(k),qatt(i)

13. PSD calibration.
Mode: neutron single
Source: PuBe
Spectra: sqft(k) & {c1(j)<=sqtt(k)<c2(j)] ; k=1 - 32, j=1 - 3
qtot(i), qfst(i), qfst(i) vs qtot(i) ; i=1 - 64
Analyse: the spectra fitting the PSD separation line through the valley between the neutron and gamma peaks (n_GAMMA_cut).

APPENDIX IV.

The introductory comments for the calling sequence of the programs used for the calibration of the n-WALL.

```
C ***************************************************************************
C *                                                                         *
C *                        Program PEAK_fit.for                             *
C *                                                                         *
C *                        Z. Seres, MSU 14/08/97                           *
C *                                                                         *
C ***************************************************************************
C
C The program PEAK_fit performs peak searching using cross correlation method
C     and a Gaussian peak fit
C There is a possibility to give a type identifier written to the output
C     preceeding the peak parameters
C
C Files used:
C       sys$input       Conversation
C       for006          Messages
C       for011          Spectrum input (LMDP FORTRAN binary file
C                         containing one-dimensional 2k spectra of the
c                         same kind (type) for a series of cells
c                       spectra can be skipped
c                       the sequence number of the first cell
```

```
c                       and the number of the cells to be analysed requested
C       for012          TOPDRAWER file of the fits (LASER.TOP)
C       for021          Summary table (LASER.TAB)
C       for022          Tracing protocol on request (LASER.PRT)
C
C Peak searching parameters: sigma=2 and 8 ch  (time/pos, charge)
C                       window=5 and 16 ch
C                       discrimination=2 (background factor)
C
C Input parameters:
C Title (comment)
C Spectrum type:        1 - 7 (7 end)
C Spectrum filename:    separate files
C Cycle definition:     number of cells
C                       sequence number of the 1-st cell, and number of cells
C                       to be skipped
C
C Input spectrum:       LMDP binary 1 dimensional spectra
C                       (separate files read one by one)
C
```

```
C ************************************************************************
C *                                                                      *
C *                        Program CMPT_edge.for                         *
C *     performs the Compton edge fits using cross correlation method    *
C *                                                                      *
C *                        Version MSU 8/24/97                           *
C *                             Z. Seres                                 *
C *                                                                      *
C ************************************************************************
C
C       Program actions:
C          1. Reads a one dimensional spectrum
C               in LMDP form written by SARA3 with USER option=6
C          2. Performs a sliding fit of the searching function
C               Fermi function of unit amplitude and given diffuseness
C                   f(k)=1/(1+exp(k/sigma))
C                   sigma=sigma0+0.001*k adjusted
C               the fit is applied in a given window channel number
C          3. Produces a .TOP plot file of the spectrum and fit results
C
C       Files used:
C               SYS$INPUT interactive control conversation
```

```
C              for006    messages
C              for011    spectrum input file
C              for012    output .TOP file (has to be assigned)
C              for022    output .TAB file for code nWALL_Ecal
C                           (energy (MeV), Compton edge)
C
C       Parameters asked:
C              n: length of the spectrum (to be fitted)
C              sigma0: diffuseness of the Fermi funtion (in channel number)
C              m: searching window width (approx. 2*sigma0)
C
```

```
C*****************************************************************************
C                                                                             *
C                        Program nWALL_Ecal.for                               *
C      performs energy calibration of the active PMTs of the nWALL            *
C      from gamma-source measurements and suggests modified HV table          *
C                                                                             *
C                     Version MSU  8/6/1997                                   *
C                         Z. SERES                                            *
C                                                                             *
C*****************************************************************************
C
C     Program actions:
C        1. Read hv.usr file with active flags and HV values
C             [Five comment lines with: 2006 format(a64)}]
C             [Data with: 2007 format(i4,i10,4x,a4)]
C             Convention: #PMT sequence number LEFT, RIGHT from bottom to top
C                         first wall, second wall (all 100)
C                         active #PMT > 0, not used #PMT < 0
C                       HV input active PMT-s in sequence order (from ch 0)
C                       #Logical number: patch panel sequence (BANK1, etc.)
C                         LEFT and RIGHT separated CFD units
C        2. Read files of Compton edges
C             [Active PMT sequence number, Compton edge, energy with
C               2001  format(2i6,f10.4)]
C        3. Read pedestal file (empty: NONE)
C             [Three comment lines with: 2006   format(a64)}]
C             [Q_tot pedestals with: 2080   format((8x,8(i5,1x)))]
C        3. Calculate linear regression: E=C0+C1*Ai (for every active PMTs)
C             (at least 2 values required for a PMT)
C             pedestal <= 0 ignored; modified pedestals are suggested
C             see end of ENERGY.CAL file
```

```
C        4. Gives suggested HV values for even amplification wanted (optional)
C             Output: hv.usr form
C             For XP4312B PMT-s: dV=267*ln(C1w/C1) is used
C
C     Files used (name convention: capital means mandatory or given name):
C             SYS$INPUT  interactive control conversation
C             for006     messages
C             for011     gamma calibration files (co.cmpt) (max. 10)
C             for013     PMT active flag & HV setting old (hv.old)
C             for014     Pedestal's file (qtot.ped)
C             for021     HV suggested (HV.NEW)
C             for022     energy calibration (ENERGY.CAL)
C
C     Input:  Amplification wanted (C1w in MeV/ch)
C
C     Parameters built in:
C             # of PMT-s (kpmt=100)
C             dE/dV PMT sensitivity (DedV=267) from XP4312B data sheet
C             PMT-s are active if hardware sequence number is >0
C                      inactive 0< hardware sequence number
C


C ***************************************************************************
C *                                                                         *
C *                      Program n_GAMMA_cut.for                            *
C *                  Version 2-nd order polynomial fit                      *
C *                                                                         *
C *                       Z. Seres, MSU 30.03.99                            *
C *                                                                         *
C ***************************************************************************
C
C The program n_GAMMA_CUT.for determines a 1-st or 2-nd order polynomial
C    n/gamma cutting line in
C    the geometric mean pulse shape discrimination scatter plot
c    performing automatic peak searching in Q-head spectra
c    measured by Q-tot conditions using cross correlation method
c    and makes two Gaussian peak fit, calculates the merit of the
c    PSD
c Attention the sequence of spectra: Cell1-32 low, Cell1-32 medium,
c       Cell1-32 high !!!!!
C
C Files used:
C       sys$input       Conversation
```

```
C       for006          Messages
C       for011          Spectrum input (LMDP FORTRAN binary file
C                       containing 2 or 3 * #CELL one-dimensional 2k
c                       Q_head spectra e.g.: for 1 MeV , 1.5 MeV,
C                       and 4 MeV slices in a cell)
C       for012          TOPDRAWER file of the fits (PSD.TOP)
C       for021          Cutting line parameter file (PSD.CUT) for
C                          lexicon file editing
C       for031          Summary table (PSD_CUT.TAB)
C       for022          Tracing protocol on request (PSD.PRT)
C
C Input parameters:
C Peak searching parameters: sigma=8 and 10 ch  (L, M/H)
C                       window=10 and 12 ch
C                       discrimination=2 (times the background)
C Spectrum filename
C Cycle definition:     number of cells and number of Q_tot bins
C                       sequence number of the 1-st cell, and number of cells
C                       to be skipped
C Bin definition:       Q_tot bin centers (ch)
C
C Input spectrum:       LMDP binary 1 dimensional spectra
C                       spectrum sequence: Low cut, High cut times #cells
C
```

FIGURE CAPTIONS

Fig. 1. Measured left *Time* vs geometric mean of total charge (*sqtt*) in cell 2 biased individually. Cross talk peak at (0, 885) when cell 3 was biased.

Fig. 2. Laser *Time* peak in cell 2 biased individually. Time resolution is 0.7 ns FWHM.

Fig. 3. Light propagation measured with collimated ^{60}Co and ThC" sources [2].

Fig. 4. Position spectrum of a point like laser excitation. The position solution is 5.5 cm FWHM for ≈ 5 MeVee pulses.

Fig. 5. Position spectra of laser+cosmics background in cell 2 biased individually. Upper panel with nominal *dt* values, lower one *dt* tuned symmetrically left and right ($+0.5, -0.6$ ps/channel).

Fig. 6. Calibrated time spectrum of left PMT of cell 2 in neutron single mode. Time resolution of self stopped peak is ≈ 1 ns FWHM.

Fig. 7. n/γ separation line fit for cell 2. The upper panels are geometric mean spectra of fast component gated by narrow windows in geometric mean of total charges measured with PuBe source.

Fig. 8. Position dependence of total charges left and right measured by the Compton edges. a.) PuBe γ-ray spectra with position cuts in cell 6, b.) with collimated ^{60}Co in cell 7 of the second wall [2].

Fig. 9. Position dependence of the geometric mean of charges shown in fig. 8. a.) *sqtt*, b.) $sqft$ with PuBe position cuts, c.) cell 8, d.) with collimated ^{60}Co source.

Fig. 10. Calculated position dependence of charge at one end of a circular tube of $r = 3.5$ cm, $\vartheta_c = 41.5^o$, $\lambda = 180$ cm, and $P = 0.88$ and $P_n = 0.6$.

Fig. 11. Calculated position dependence of the geometric mean of charges shown in fig. 10.

Fig. 12. PuBe γ-ray spectra without (*sqtt*) and with (*cqtt*) position correction.

Fig. 13. The effect of the position correction in the scatter plot of PuBe γ-ray spectra.

Fig. 14. Position spectra of γ-rays and neutrons with hardware and *Eeeq* energy thresholds.

Fig. 15. The effect of position correction on PSD. The geometric mean of the fast component gated by narrow windows of geometric mean of total charges without correction ($sqft$ vs *sqtt*) and with correction ($cqft$ vs *cqtt*) at 1 MeVee.

Fig. 16. a.) Energy calibration of the geometric mean of the $x = \pm 10$ cm middle section of cell 2 and b.) the CAN detector with ^{60}Co, ThC", PuBe γ sources.

Fig. 17. γ spectra measured with the CAN and equivalent sections ($x = \pm 7.6$ cm full and $x = \pm(80 \pm 7.6)$ cm dashed lines).

Fig. 18. Neutron spectra as in fig. 17. The CAN spectrum seems to be expanded.

Fig. 19. Ratios of the spectra normalized to the equivalent middle cell section. The cell neutron ratios are constant corresponding to the solid angle (0.80), the γ somewhat larger because of the cosmics background.

Fig. 20. The γ ratio for the CAN detector is constant about 0.8, however, the neutron ratio is growing because of the strong nonlinearity calibrating with γ sources. The triangles show the ratios with proton energy correction.

Fig. 21. Neuton and γ-ray relative efficiencies between 1–4 MeVee of 10 cm long sections as a function of position. The curves are calculated relative solid angles.

Fig. 22. The same as fig. 21 for the first and second wall with closer source-detector distance.

Fig. 23. Relative efficiency dependence on the detector length.

Fig. 24. PuBe γ and neutron spectra with proton calibration for the CAN detector.

Fig. 25. PuBe neutron/γ discrimination in $cqft$ vs $Eeeq$ representation with hardware cut 6×5.5 mV.

Fig. 26. a.) PSD figure of merit, b.) n/γ peak positions, and c.) intensity spectra from fig. 25.

Fig. 27. Scatter plot $qfst$ vs $qtot$ on the left side of the PuBe source measured with the standard PSD circuit i.e. the fast component with LeCroy 2249W QDC and non terminated, oscillating emitter follower.

Fig. 28. The same as fig. 27 with terminated emitter follower. The slope of the fast component decreased by a factor 2.2 and the threshold is shifted up about 1.5 MeVee.

Fig. 29. The same as fig. 27 with the fast component measured with a Phillips 7167 QDC (12 bit). The slope remained but the threshold increased upto 1.2 MeVee.

Fig. 30. Similar to the fig. 27 but cosmics γ type events measured with a LeCroy 4300 FERA (using the total attenuated unit). The slope agrees with the standard circuits but it has a very high threshold as 7.5 MeVee.

Fig. 31. Comparison of the PSD FOM with LeCroy 2249W and Phillips 7167 ADC-s.

Fig. 32. Energy calibration of the LeCroy 4320 CFD threshold for standard HV setting (0.005 MeVee/ch).

Fig. 33. The calibration chart of the LeCroy 4303 TFC output amplitude vs FERA 4300 channel width. For help the neutron time of flight is plotted vs the energy in the lower end of the dynamic range.

REFERENCES

[1] Z. Seres, How to use the n-WALL, MSU August 26,1997, private communication.

[2] A. Galonsky, B. Perry, and Z. Seres, Efficiency of the n-WALL, MSU April 28, 1998, private communication.

[3] J.H. Heltsley, L. Brandon, A. Galonsky, L. Heilbronn, B.A. Remington, S. Langer, A. Vander Molen, J. Yurkon, J. Kasagi, Nucl. Instr. and Meth. A263 (1988) 441.

[4] J. Tőke, S.A. Masserant, S.P.Baldwin, B. Lott, W.U. Schröder, and X. Zhao, Nucl. Instr. and Meth. A334 (1993) 653.

[5] P. Zecher, D. Carter, and Z. Seres, USA Patent submitted, 1996.

[6] 16 ch CFD Type ERT 5.03.02.0, MTA ITA LAI, Foundation for Information Technology of the Hungarian Academy of Sciences, Konkoly-Thege út 29-33, Budapest, Hungary, H-1121

Fig. 1

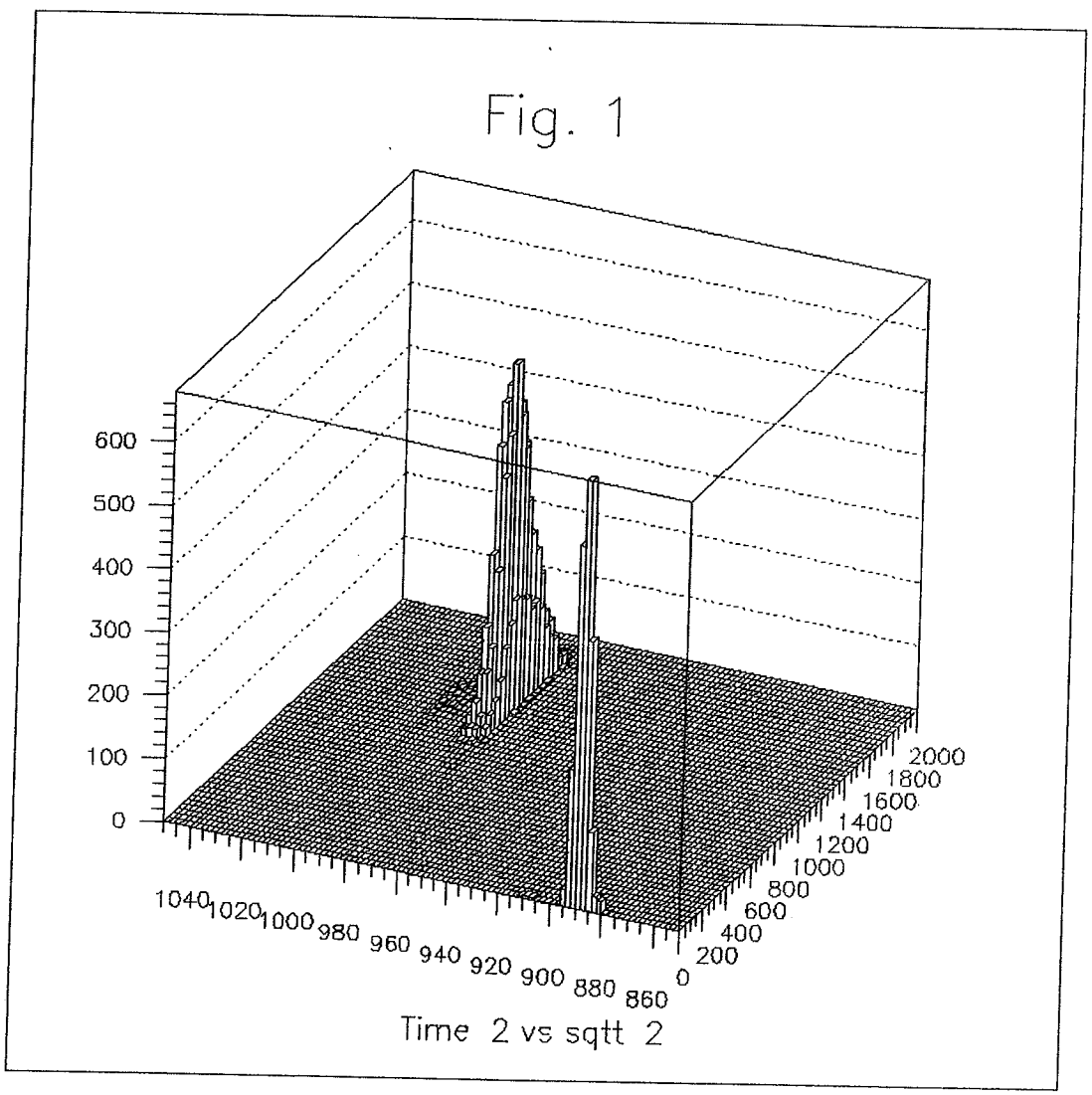
600
500
400
300
200
100
0
1040
1020
1000
980
960
940
920
900
880
860
0
200
400
600
800
1000
1200
1400
1600
1800
2000
Time 2 vs sqtt 2

Fig. 2

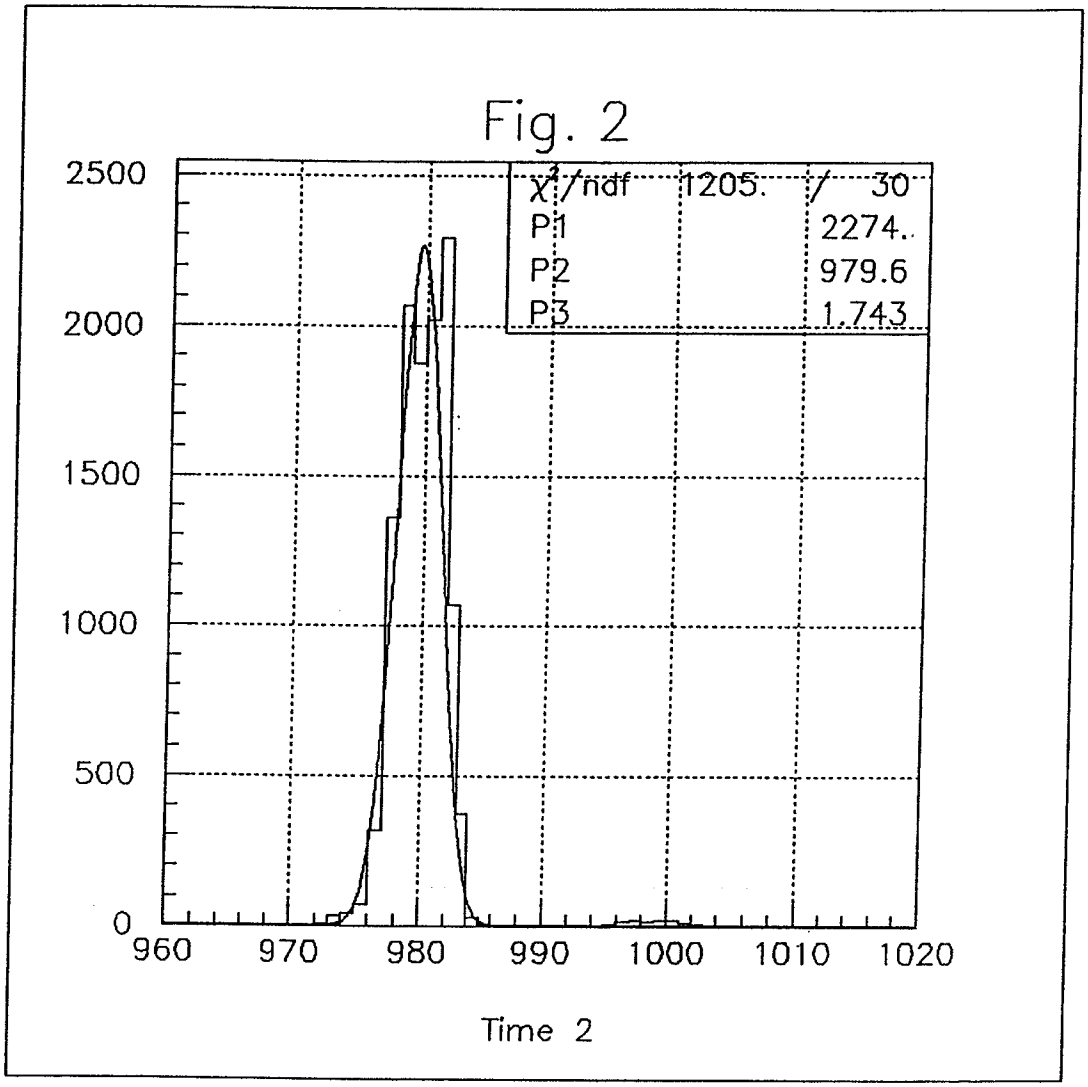
2500
2000
1500
1000
500
0
960
970
980
990
1000
1010
1020
χ²/ndf 1205. / 30
P1 2274.
P2 979.6
P3 1.743
Time 2

Fig. 3

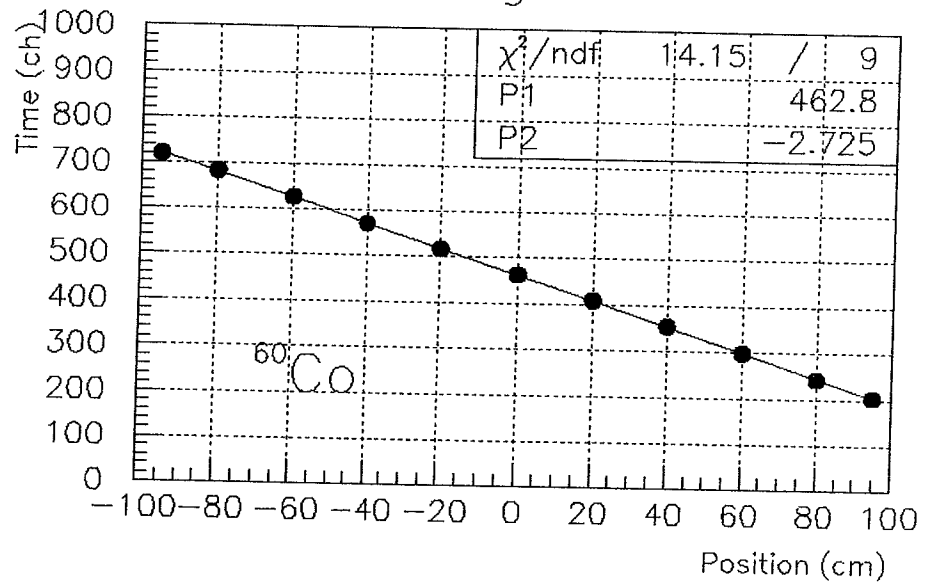
Time (ch)
1000
900
800
700
600
500
400
300
200
100
0
χ²/ndf 14.15 / 9
P1 462.8
P2 −2.725
60Co
−100 −80 −60 −40 −20 0 20 40 60 80 100
Position (cm)

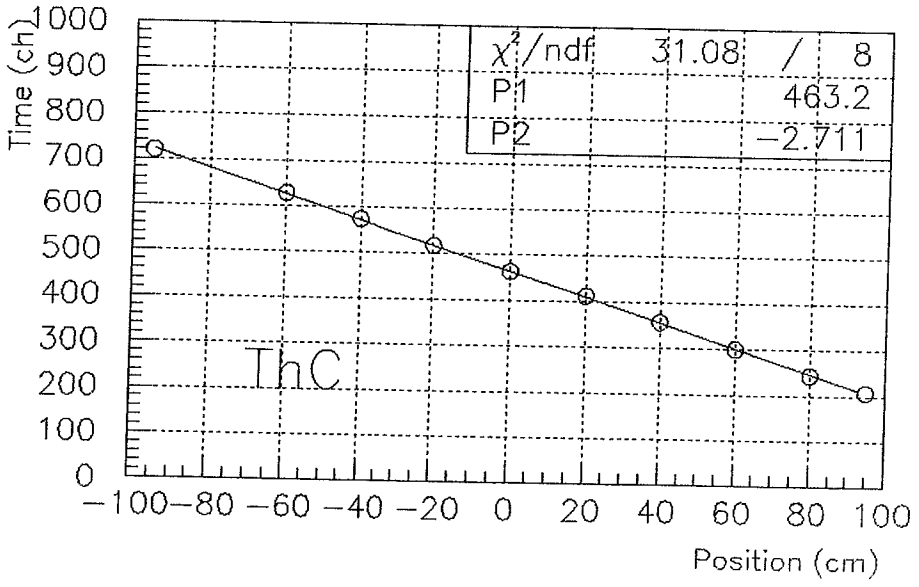
Time (ch)
1000
900
800
700
600
500
400
300
200
100
0
χ²/ndf 31.08 / 8
P1 463.2
P2 −2.711
ThC
−100 −80 −60 −40 −20 0 20 40 60 80 100
Position (cm)

Fig. 4

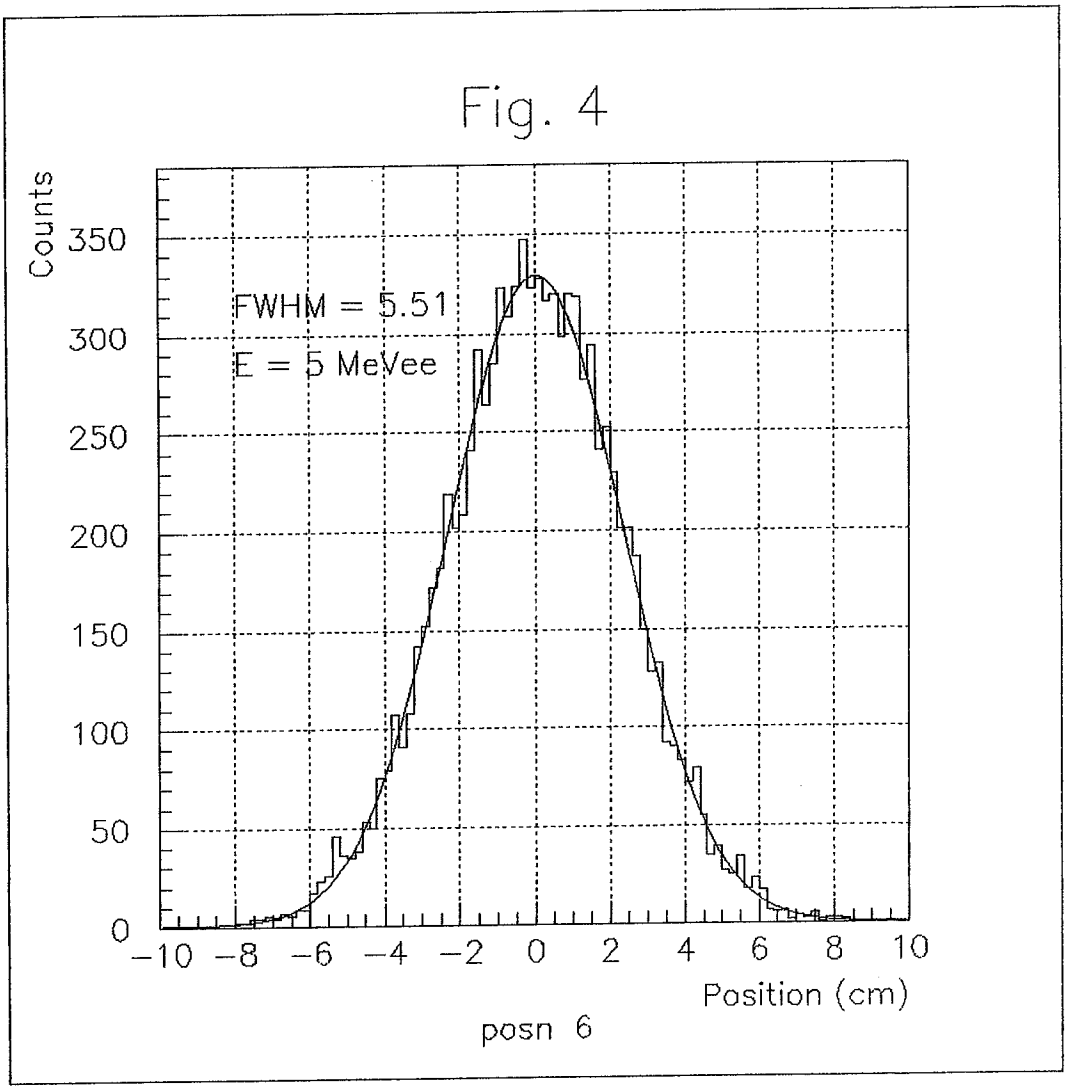
Counts
350
300
250
200
150
100
50
0
FWHM = 5.51
E = 5 MeVee
−10 −8 −6 −4 −2 0 2 4 6 8 10
Position (cm)
posn 6

Fig. 5

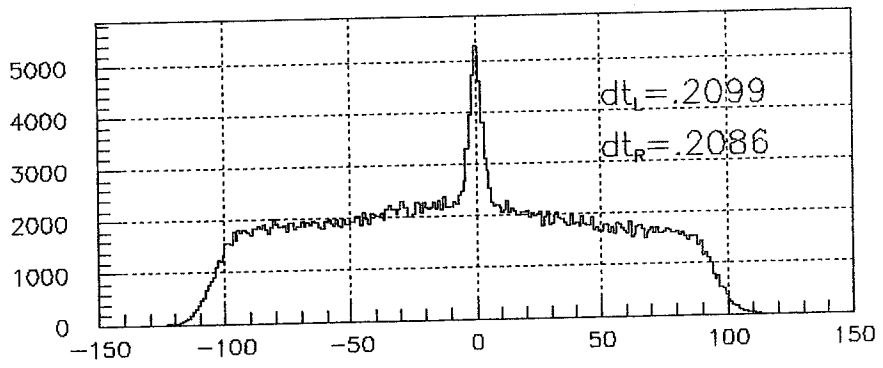

posn 6

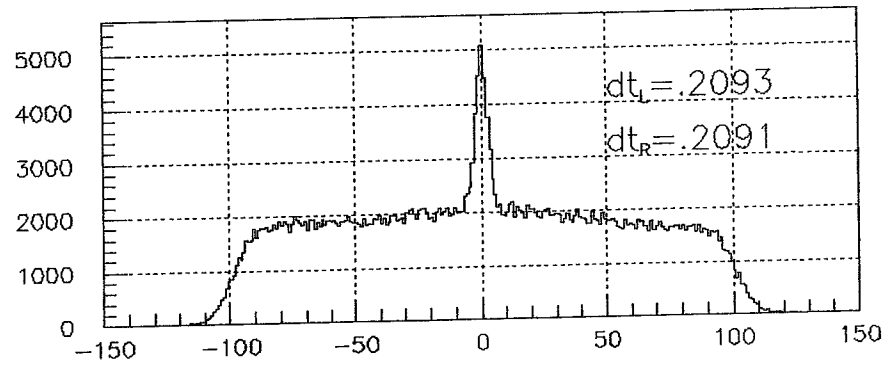

posn 6

Fig. 6

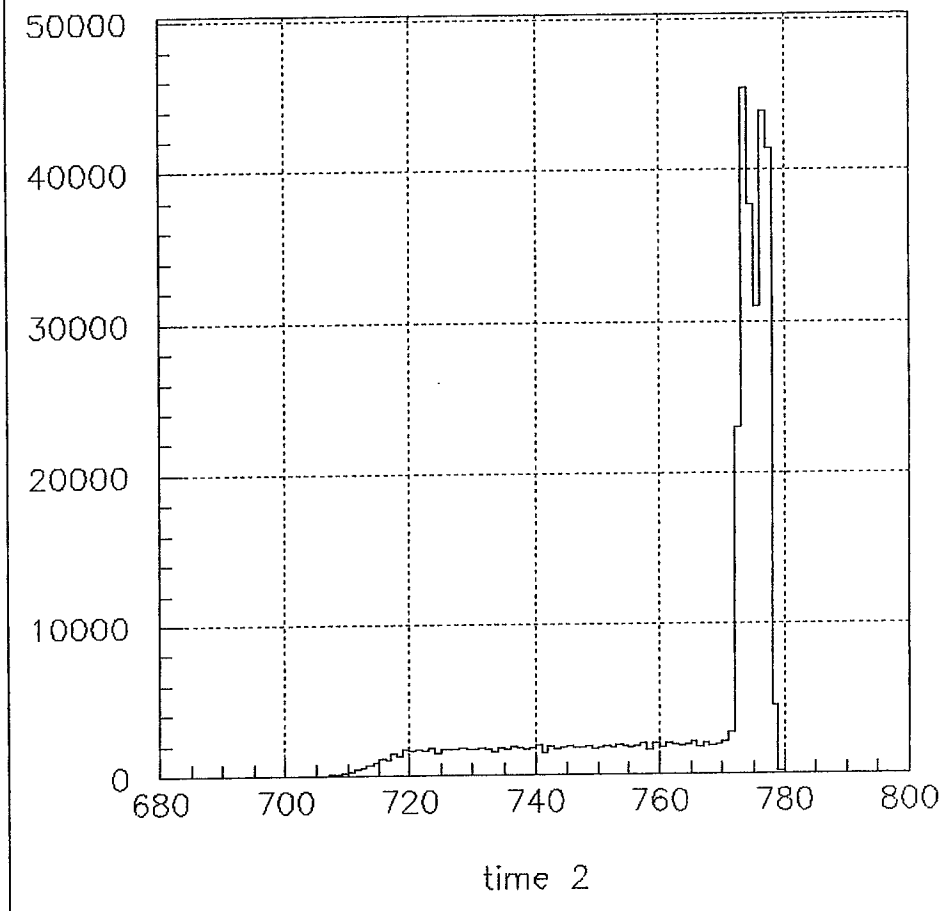
50000
40000
30000
20000
10000
0
680
700
720
740
760
780
800
time 2

Fig. 7

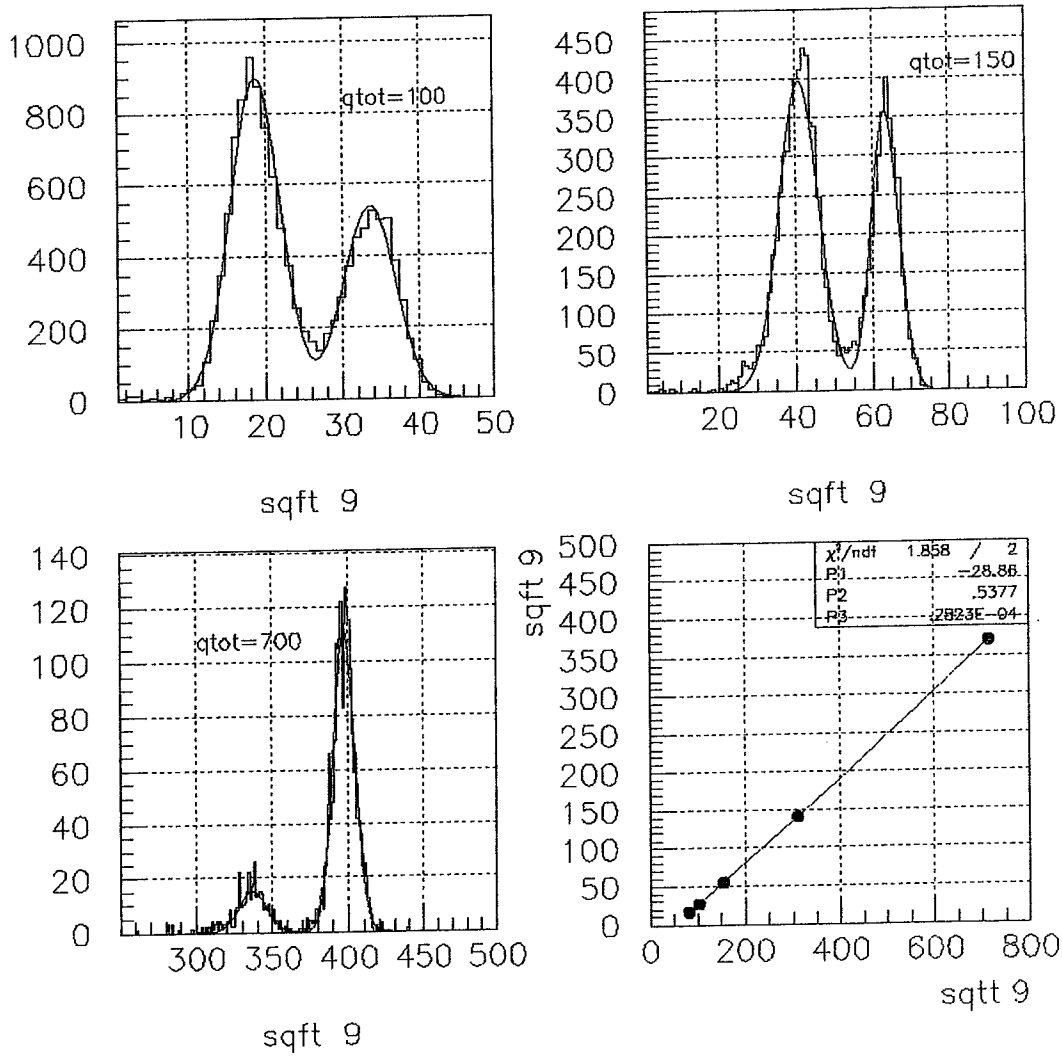
qtot=100
sqft 9
qtot=150
sqft 9
qtot=700
sqft 9
sqft 9
χ²/ndf 1.858 / 2
P1 -28.86
P2 .5377
P3 .2823E-04
sqtt 9

Fig. 8a

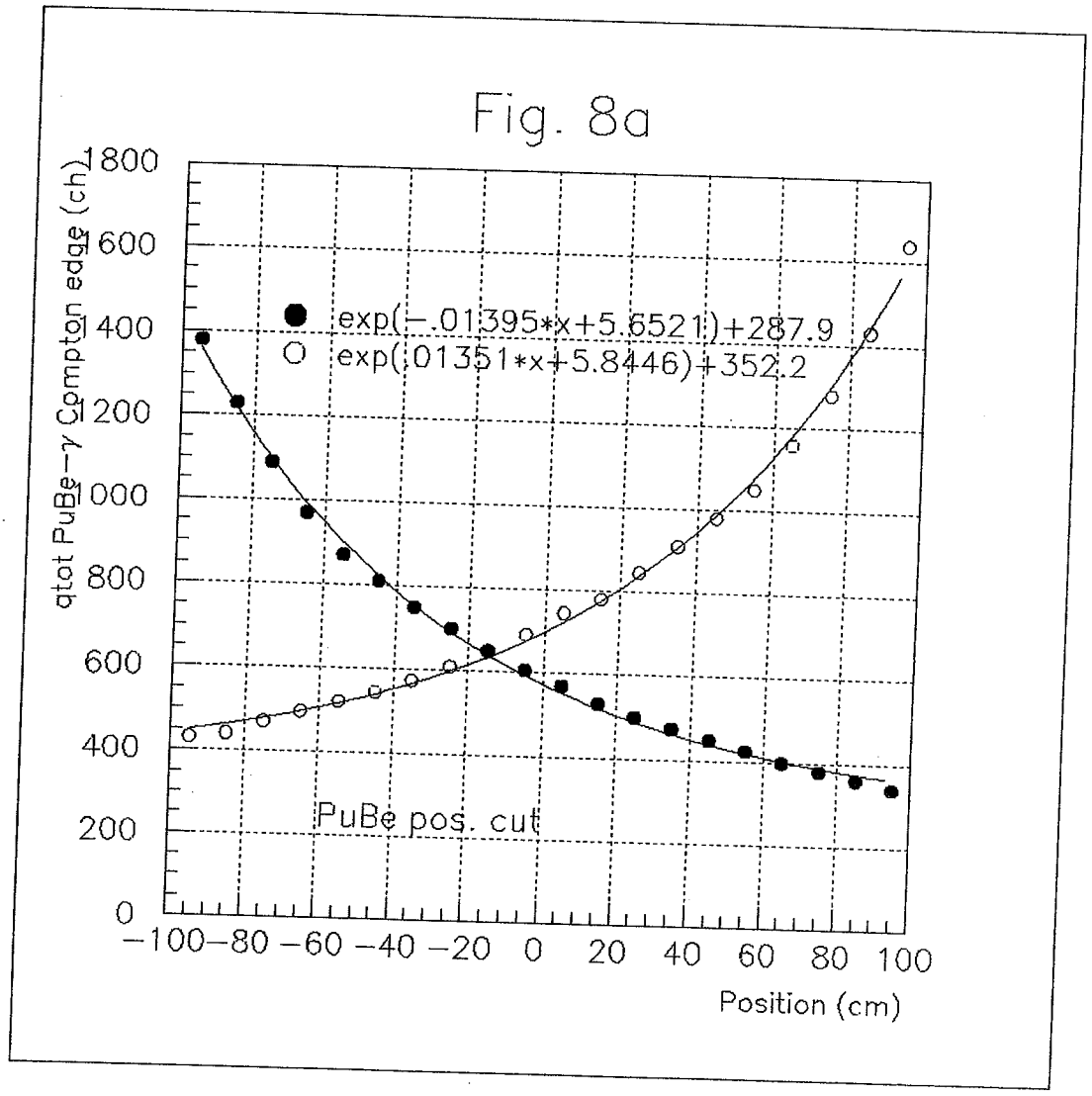
qtot PuBe-γ Compton edge (ch)
1800
1600
1400
1200
1000
800
600
400
200
0
exp(−.01395*x+5.6521)+287.9
exp(.01351*x+5.8446)+352.2
PuBe pos. cut
−100 −80 −60 −40 −20 0 20 40 60 80 100
Position (cm)

Fig. 8b

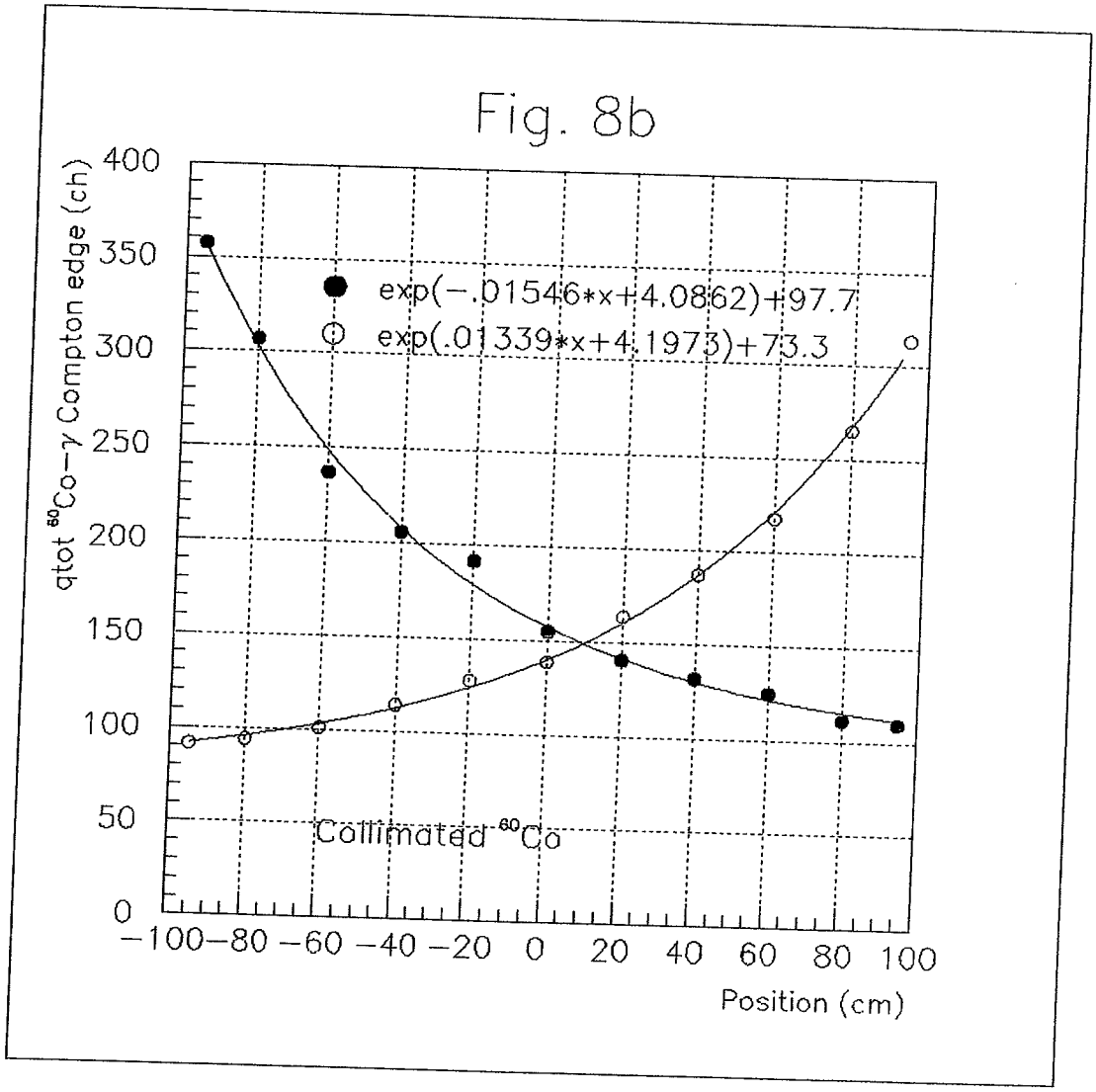
qtot ^{60}Co−γ Compton edge (ch)
400
350
300
250
200
150
100
50
0
exp(−.01546*x+4.0862)+97.7
exp(.01339*x+4.1973)+73.3
Collimated ^{60}Co
−100 −80 −60 −40 −20 0 20 40 60 80 100
Position (cm)

Fig. 9a–b

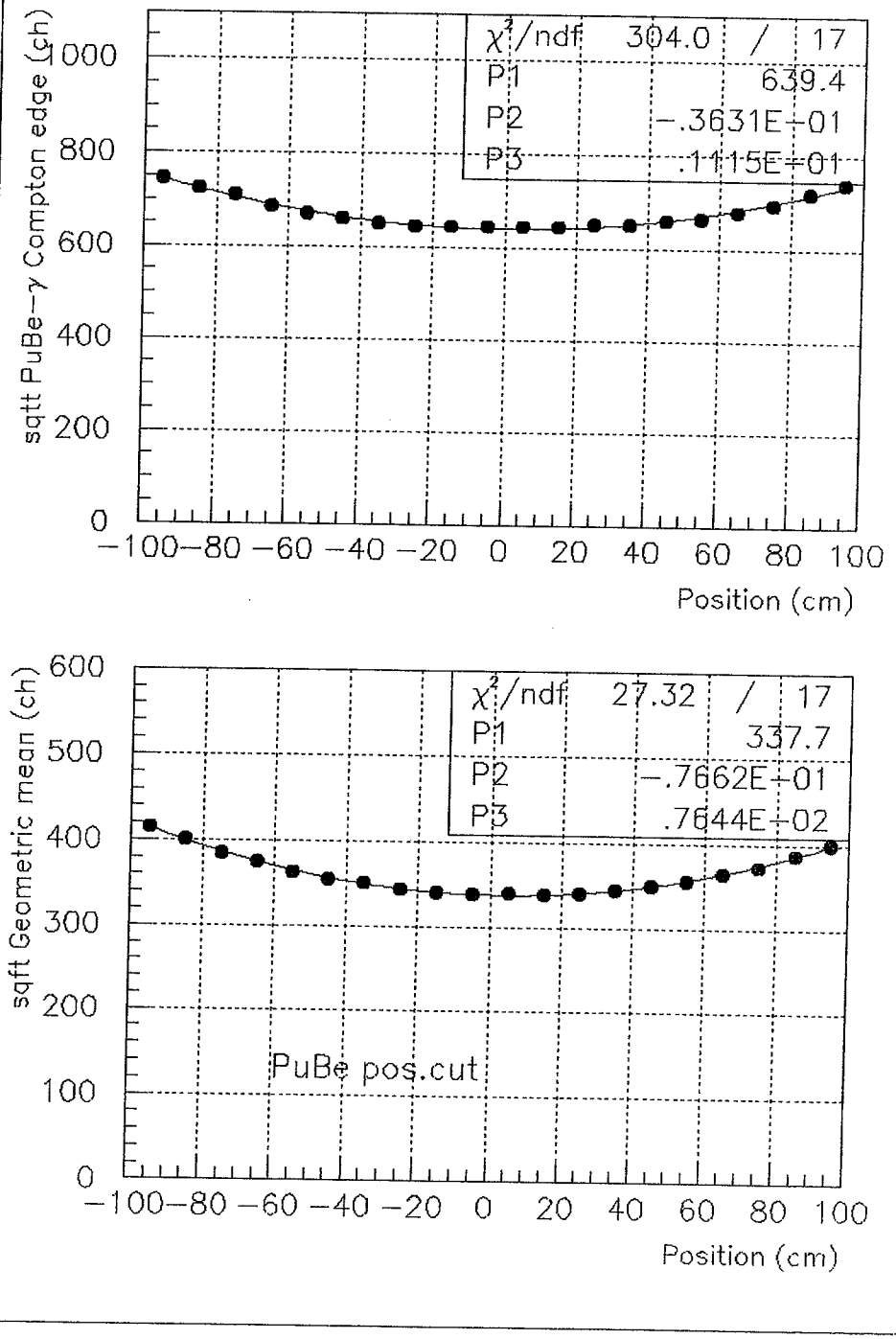
sqtt PuBe–γ Compton edge (ch)
1000
800
600
400
200
0
−100 −80 −60 −40 −20 0 20 40 60 80 100
Position (cm)
χ²/ndf 304.0 / 17
P1 639.4
P2 −.3631E+01
P3 .1115E+01
sqft Geometric mean (ch)
600
500
400
300
200
100
0
PuBe pos.cut
−100 −80 −60 −40 −20 0 20 40 60 80 100
Position (cm)
χ²/ndf 27.32 / 17
P1 337.7
P2 −.7662E+01
P3 .7644E+02

Fig. 9c–d

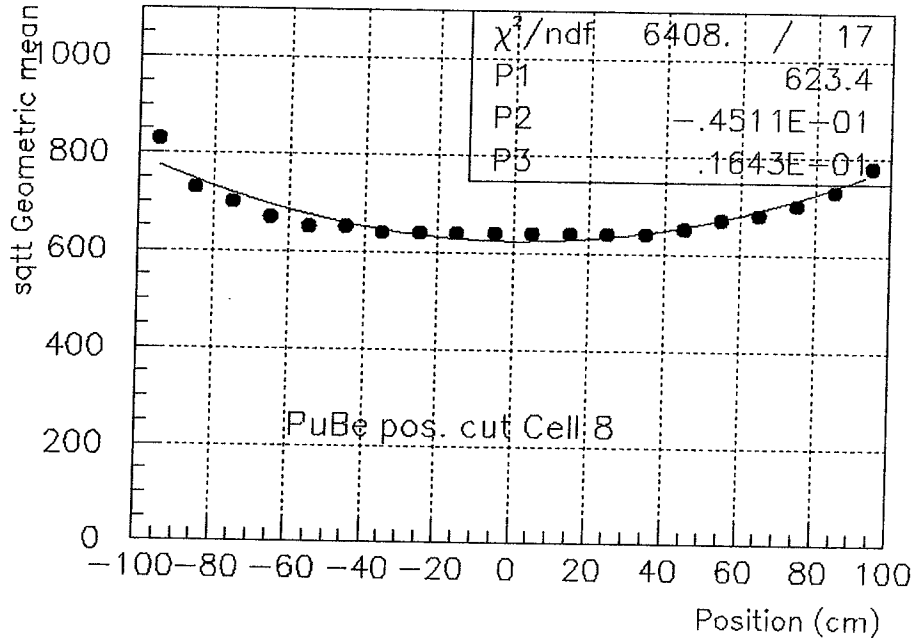
sqtt Geometric mean
1000
800
600
400
200
0
χ²/ndf 6408. / 17
P1 623.4
P2 −.4511E−01
P3 .1643E−01
PuBe pos. cut Cell 8
−100 −80 −60 −40 −20 0 20 40 60 80 100
Position (cm)

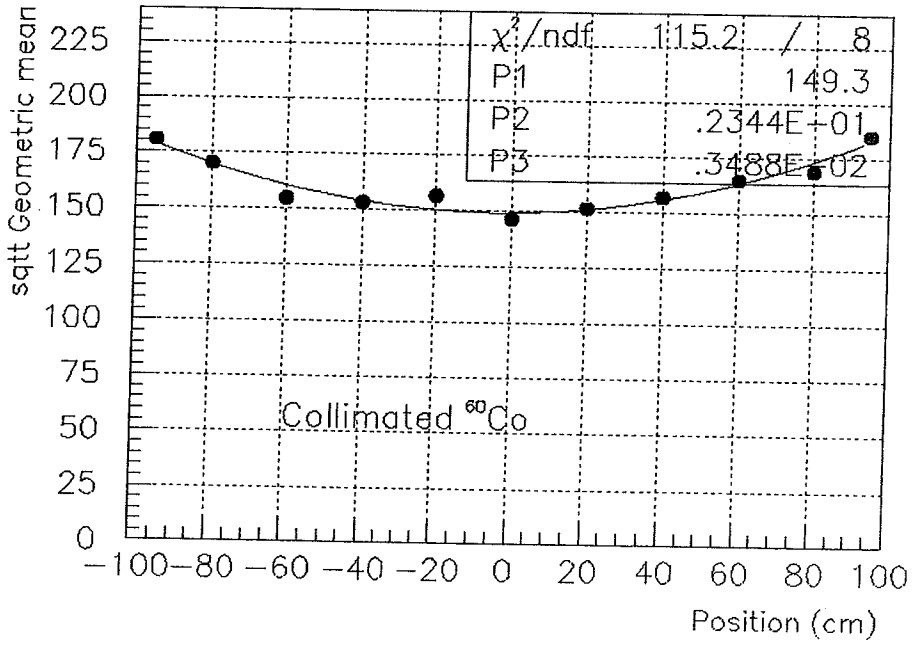
sqtt Geometric mean
225
200
175
150
125
100
75
50
25
0
χ²/ndf 115.2 / 8
P1 149.3
P2 .2344E+01
P3 .3488E−02
Collimated ⁶⁰Co
−100 −80 −60 −40 −20 0 20 40 60 80 100
Position (cm)

Fig. 10

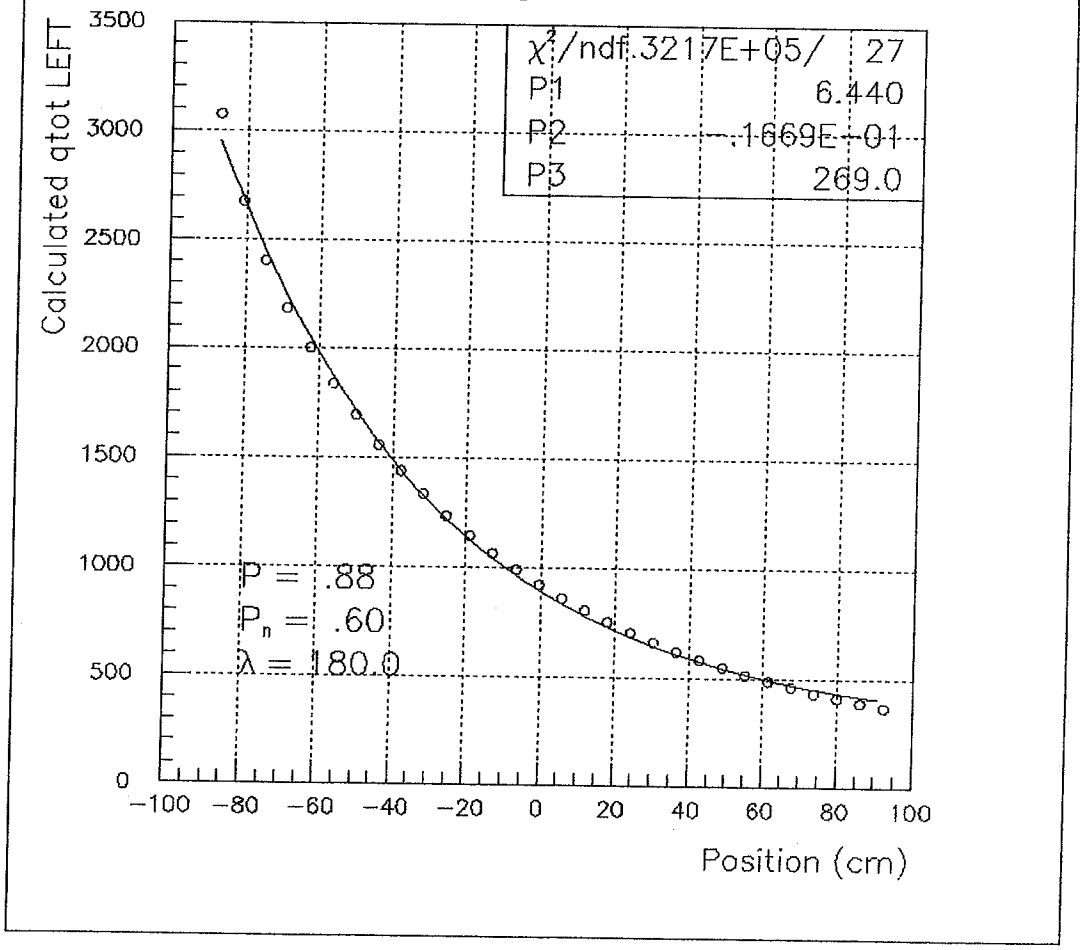
Calculated qtot LEFT
3500
3000
2500
2000
1500
1000
500
0
−100 −80 −60 −40 −20 0 20 40 60 80 100
Position (cm)
χ²/ndf .3217E+05/ 27
P1 6.440
P2 −.1669E−01
P3 269.0
P = .88
Pn = .60
λ = 180.0

Fig. 11

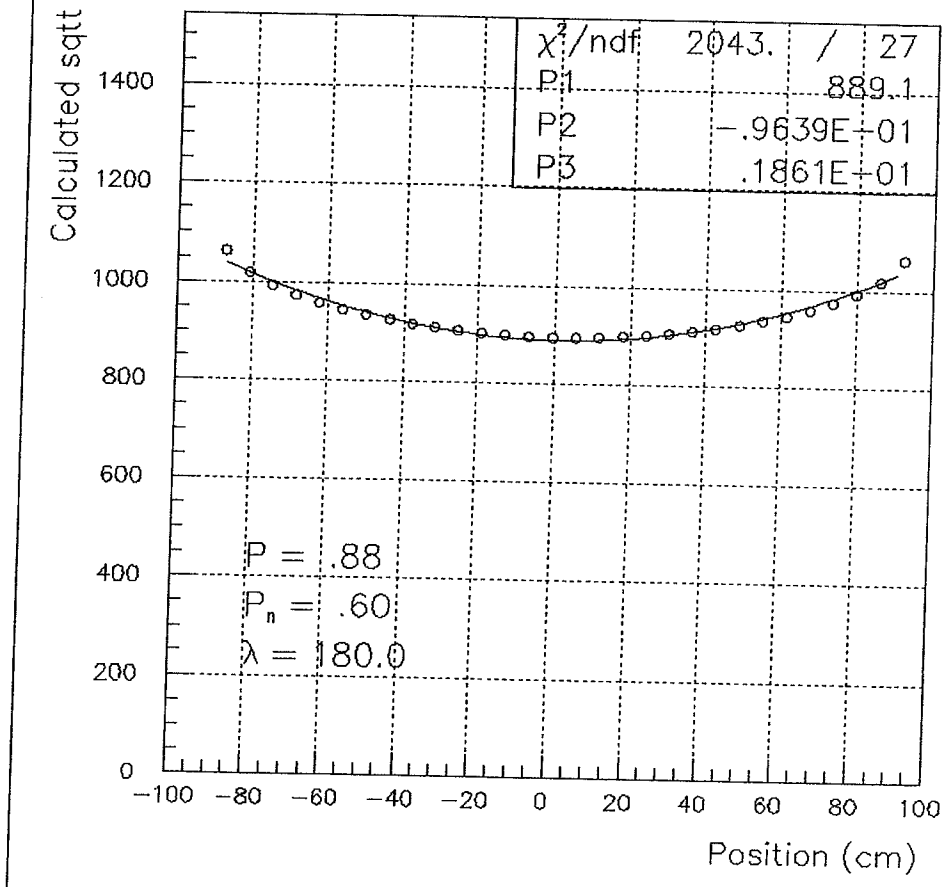
Calculated sqtt
1400
1200
1000
800
600
400
200
0
χ²/ndf 2043. / 27
P1 889.1
P2 -.9639E+01
P3 .1861E+01
P = .88
Pn = .60
λ = 180.0
−100 −80 −60 −40 −20 0 20 40 60 80 100
Position (cm)

Fig. 12

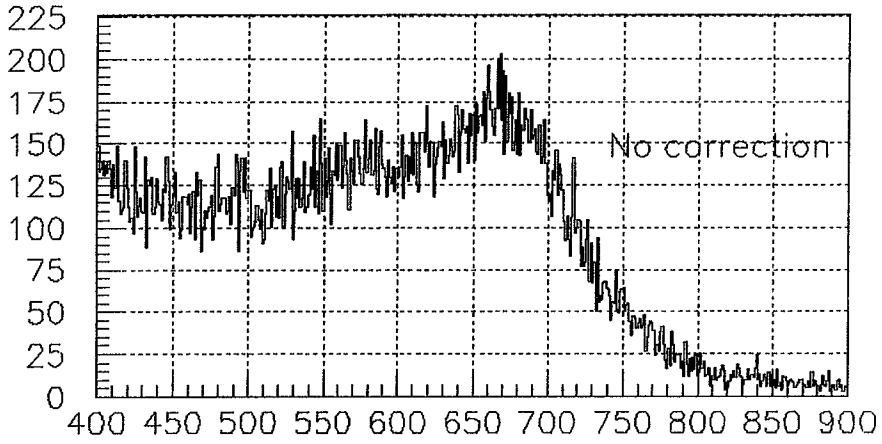
225
200
175
150
125
100
75
50
25
0
400 450 500 550 600 650 700 750 800 850 900
No correction
sqtt 2

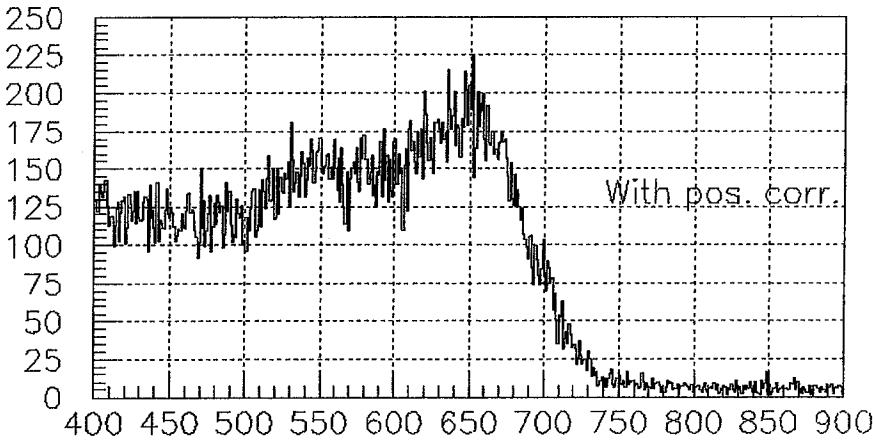
250
225
200
175
150
125
100
75
50
25
0
400 450 500 550 600 650 700 750 800 850 900
With pos. corr.
cqtt 2

Fig. 13

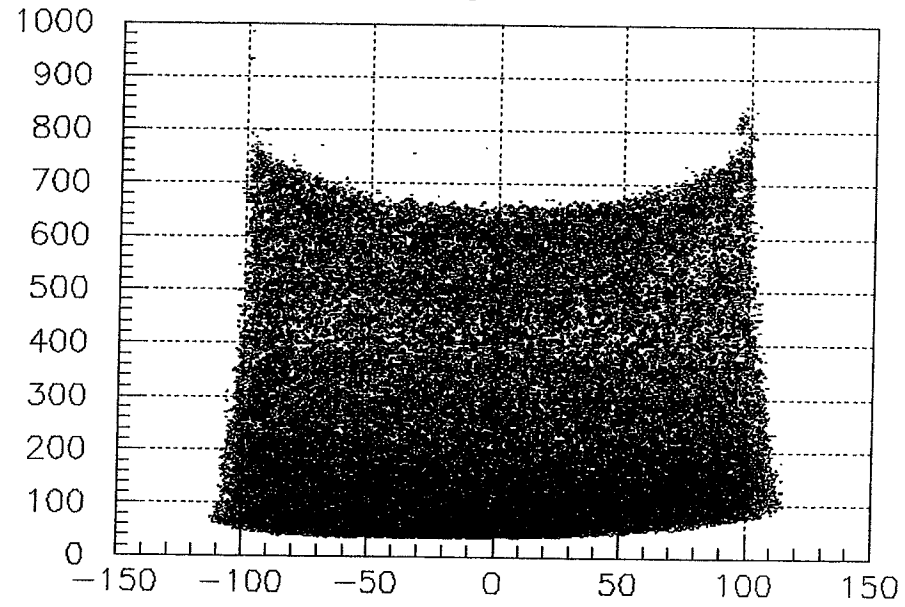

sqtt 2 vs posn 2

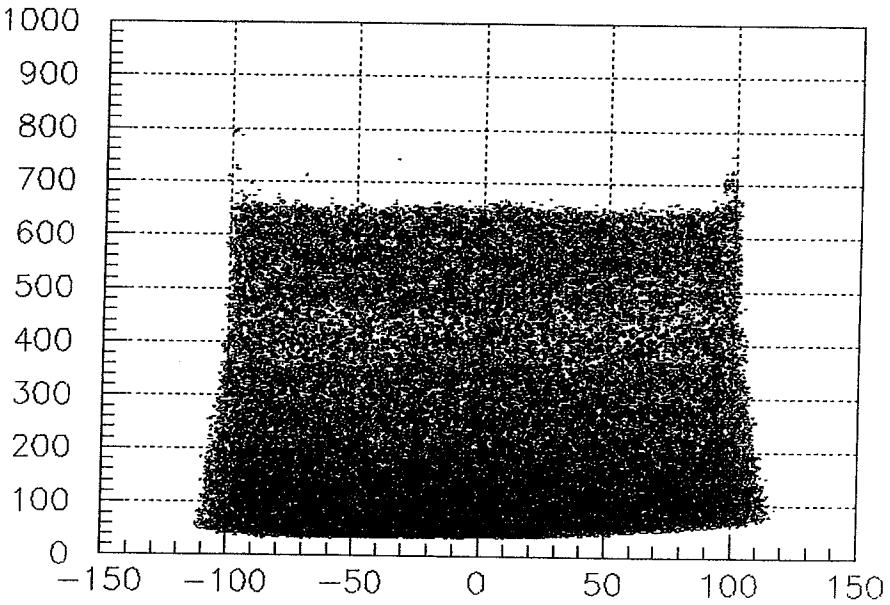

cqtt 2 vs posn 2

Fig. 14

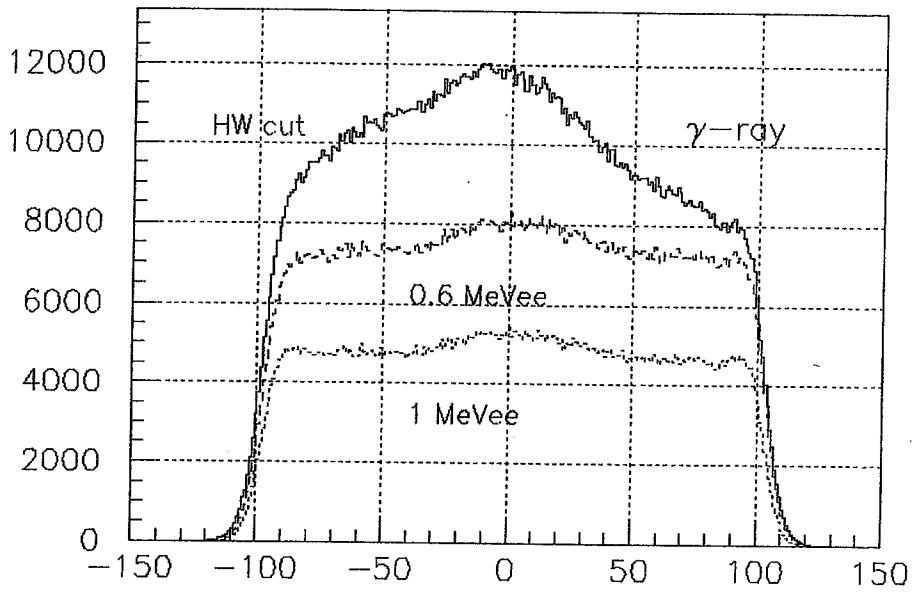
12000
10000
8000
6000
4000
2000
0
HW cut
γ−ray
0.6 MeVee
1 MeVee
−150
−100
−50
0
50
100
150
posn 2

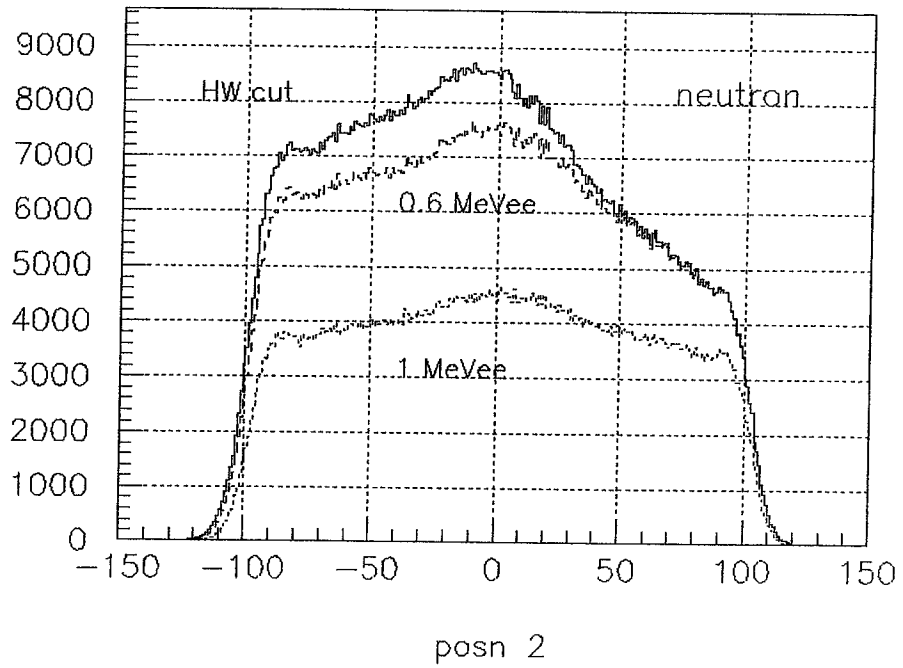
9000
8000
7000
6000
5000
4000
3000
2000
1000
0
HW cut
neutron
0.6 MeVee
1 MeVee
−150
−100
−50
0
50
100
150
posn 2

Fig. 15

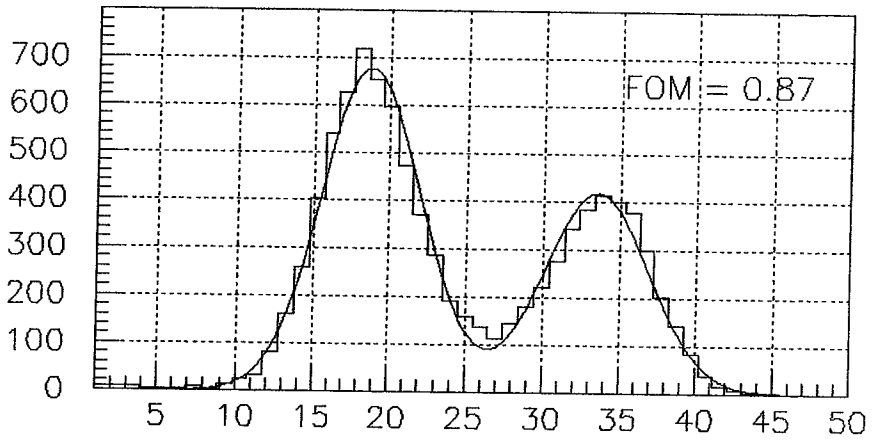

sqft 9

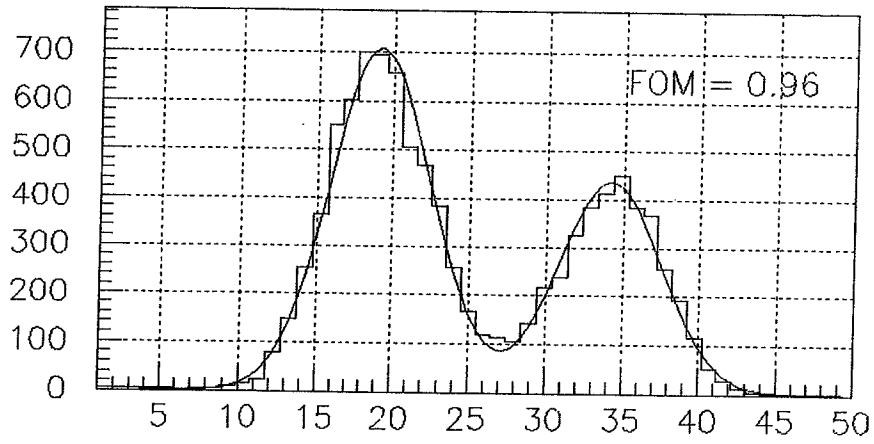

cqft 9

Fig. 16

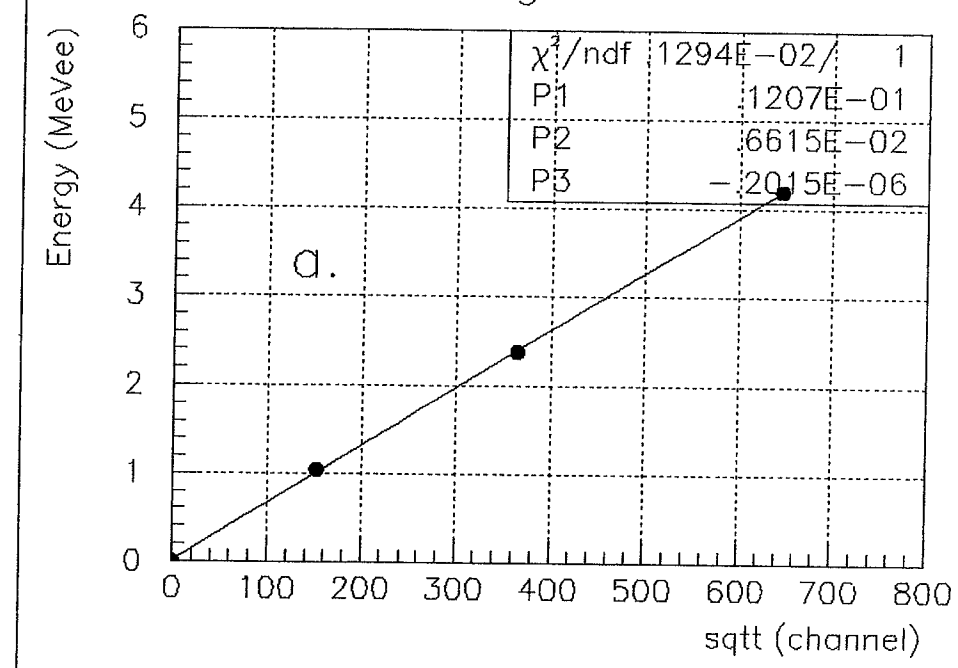
Energy (MeVee)
χ^2/ndf .1294E−02/ 1
P1 .1207E−01
P2 .6615E−02
P3 −.2015E−06
a.
0 100 200 300 400 500 600 700 800
sqtt (channel)

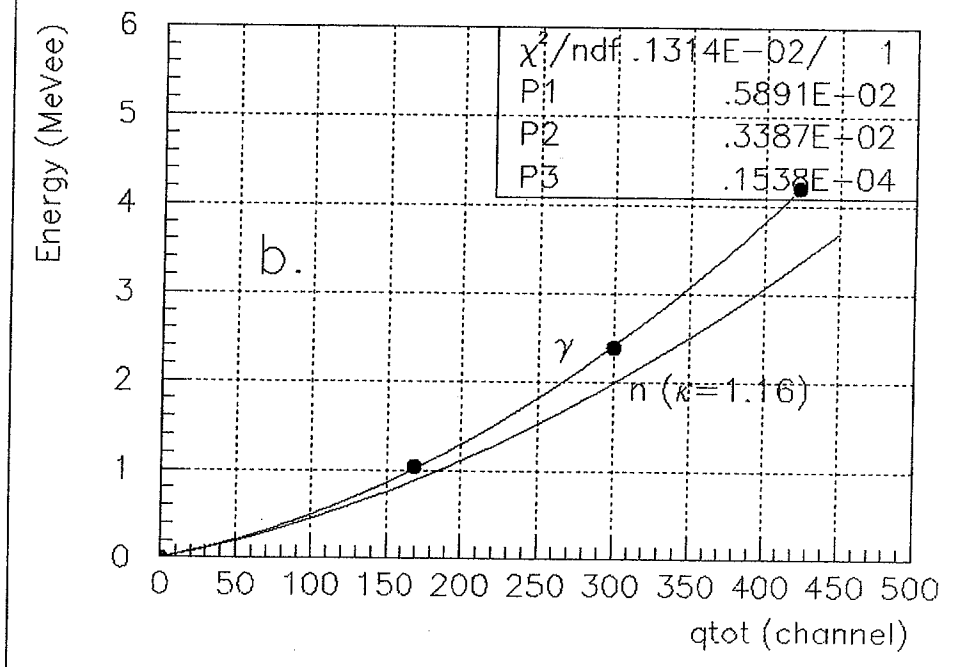
Energy (MeVee)
χ^2/ndf .1314E−02/ 1
P1 .5891E+02
P2 .3387E+02
P3 .1538E+04
b.
γ
n (κ=1.16)
0 50 100 150 200 250 300 350 400 450 500
qtot (channel)

Fig. 17

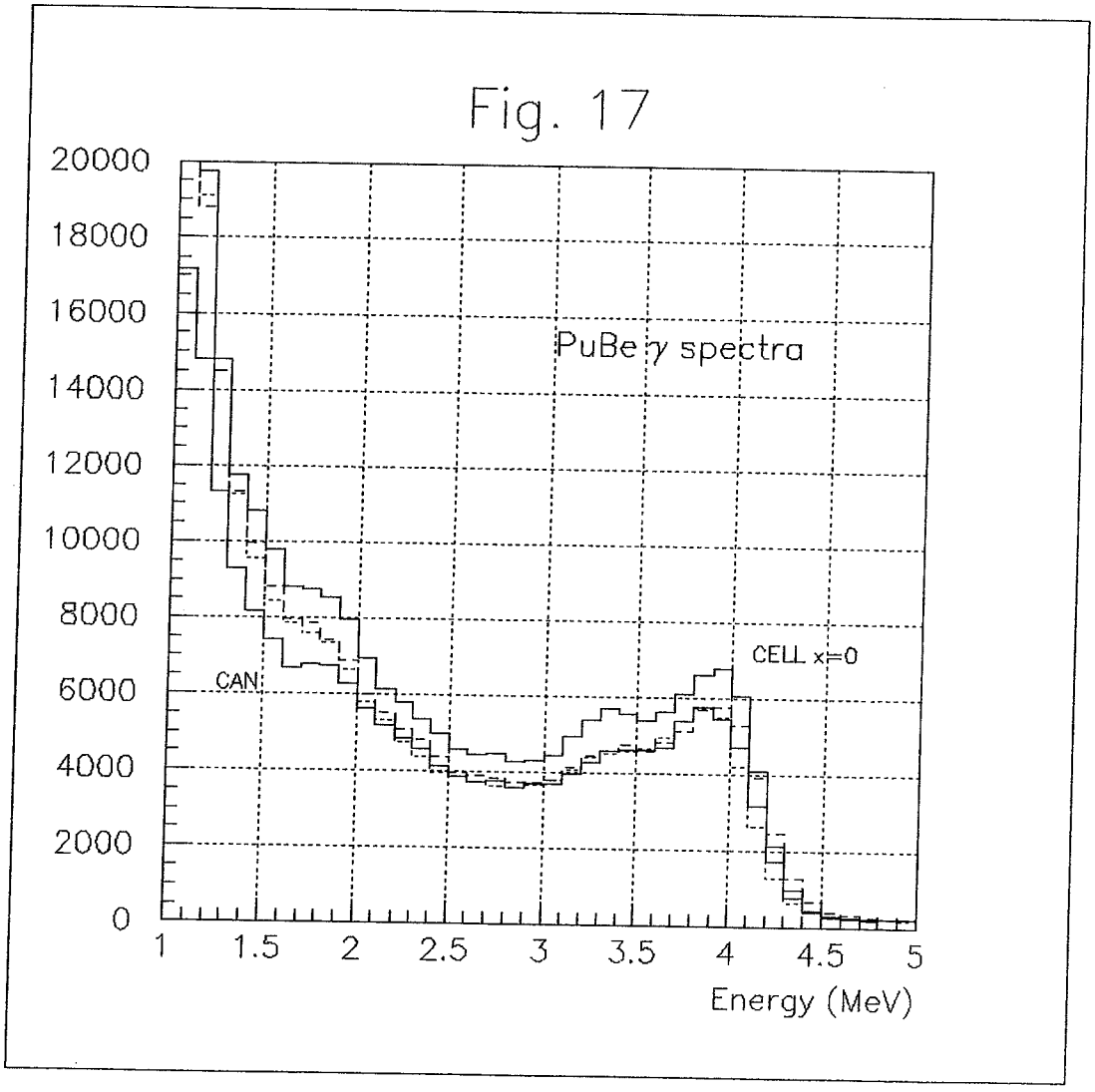
20000
18000
16000
14000
12000
10000
8000
6000
4000
2000
0
1
1.5
2
2.5
3
3.5
4
4.5
5
Energy (MeV)
PuBe γ spectra
CAN
CELL x=0

Fig. 18

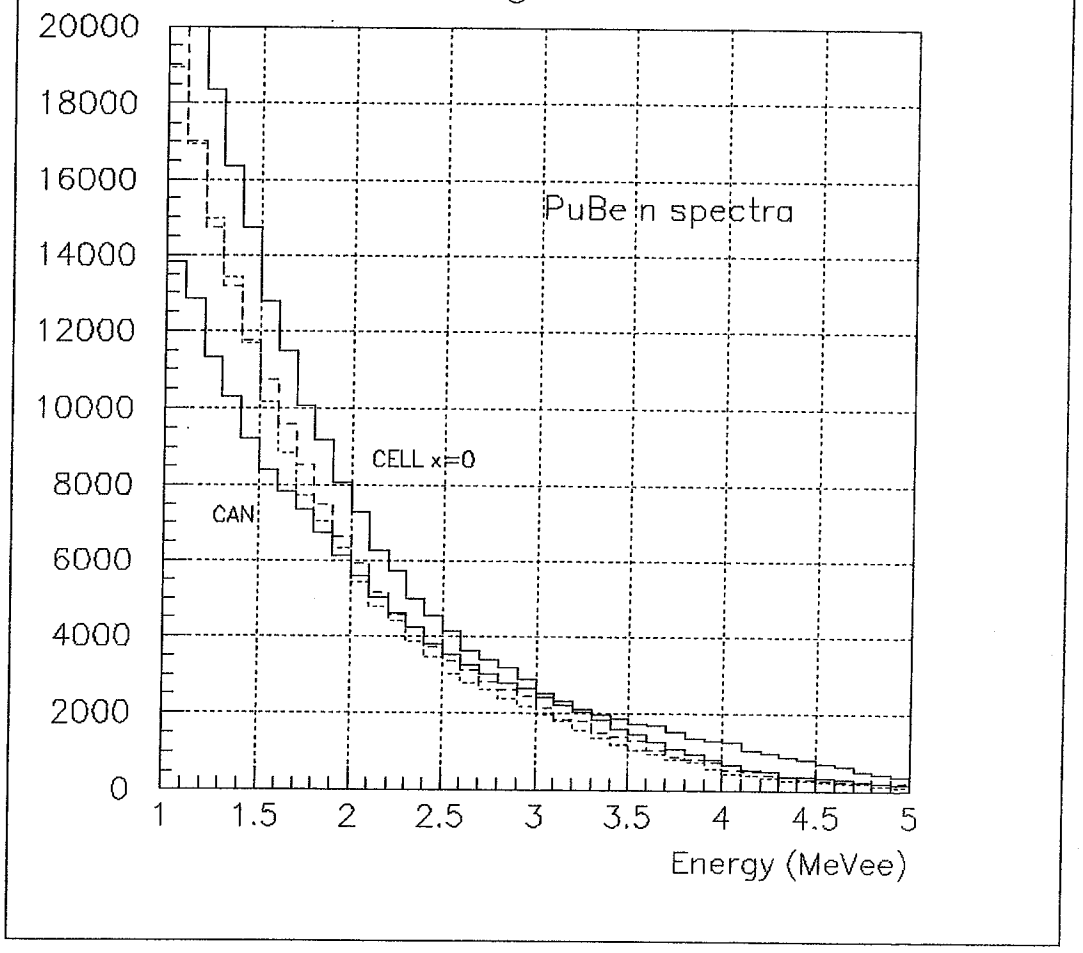
20000
18000
16000
14000
12000
10000
8000
6000
4000
2000
0
1
1.5
2
2.5
3
3.5
4
4.5
5
PuBe n spectra
CELL x=0
CAN
Energy (MeVee)

Fig. 19

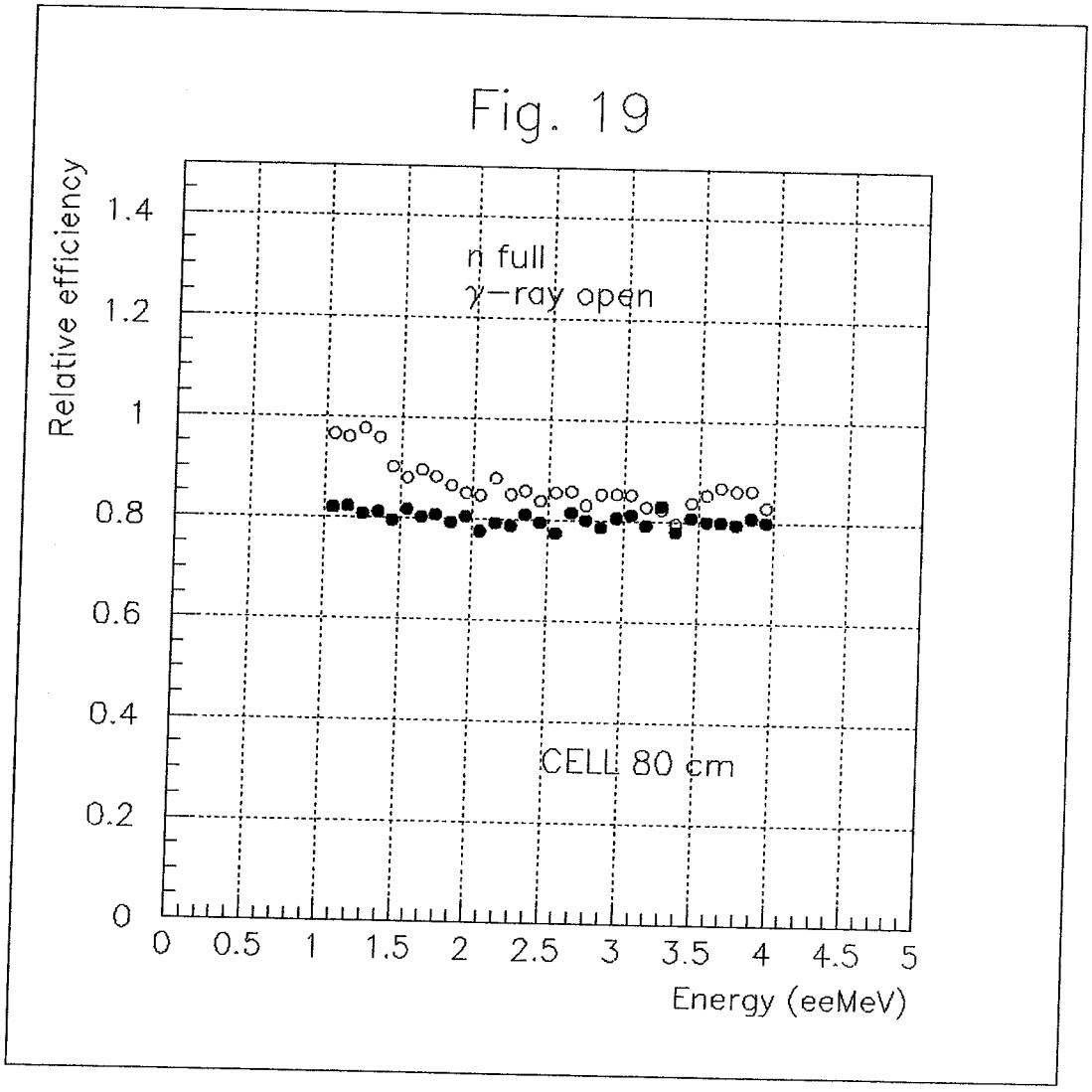
Relative efficiency
1.4
1.2
1
0.8
0.6
0.4
0.2
0
n full
γ−ray open
CELL 80 cm
0
0.5
1
1.5
2
2.5
3
3.5
4
4.5
5
Energy (eeMeV)

Fig. 20

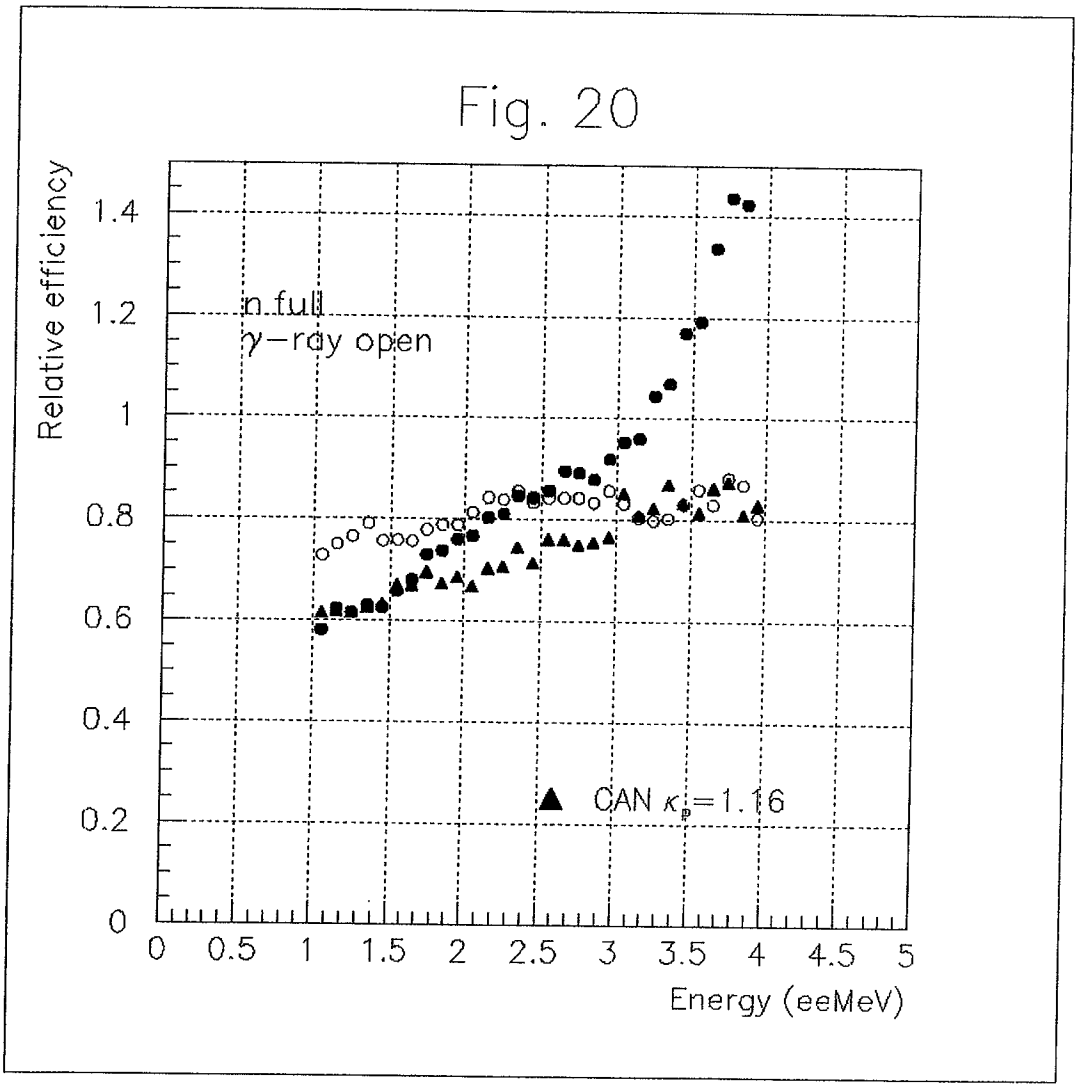
Relative efficiency
1.4
1.2
1
0.8
0.6
0.4
0.2
0
n full
γ−ray open
▲ CAN κ_p=1.16
0
0.5
1
1.5
2
2.5
3
3.5
4
4.5
5
Energy (eeMeV)

Fig. 21

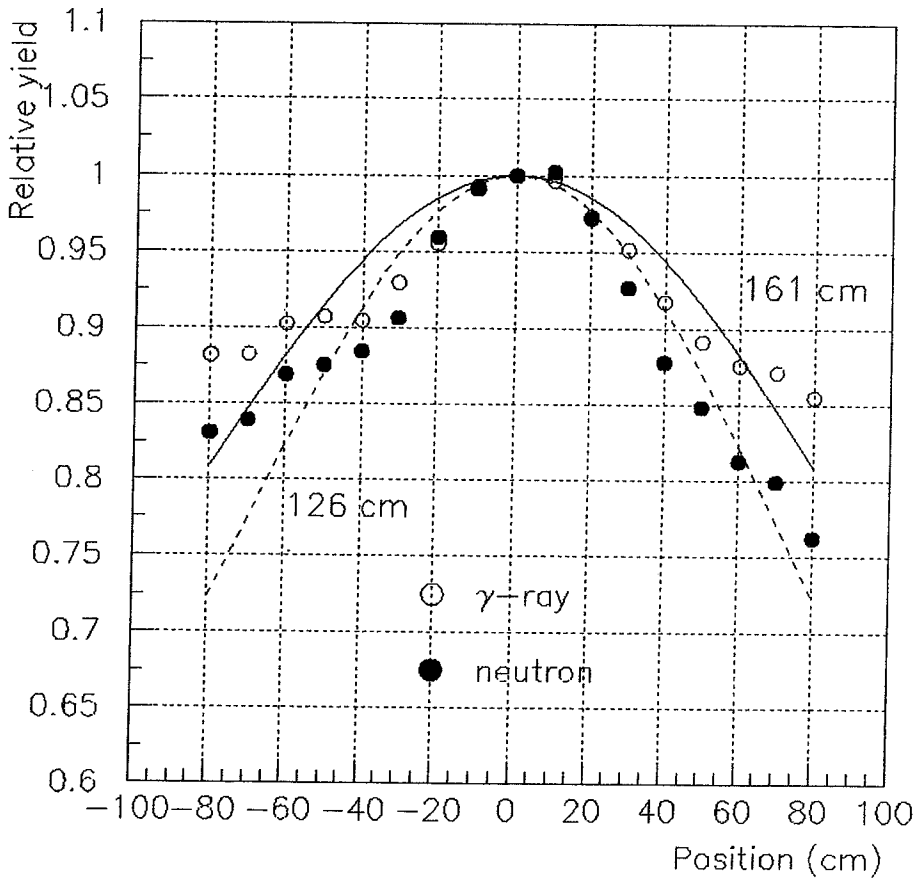
Relative yield
1.1
1.05
1
0.95
0.9
0.85
0.8
0.75
0.7
0.65
0.6
−100 −80 −60 −40 −20 0 20 40 60 80 100
Position (cm)
161 cm
126 cm
γ−ray
neutron

Fig. 22

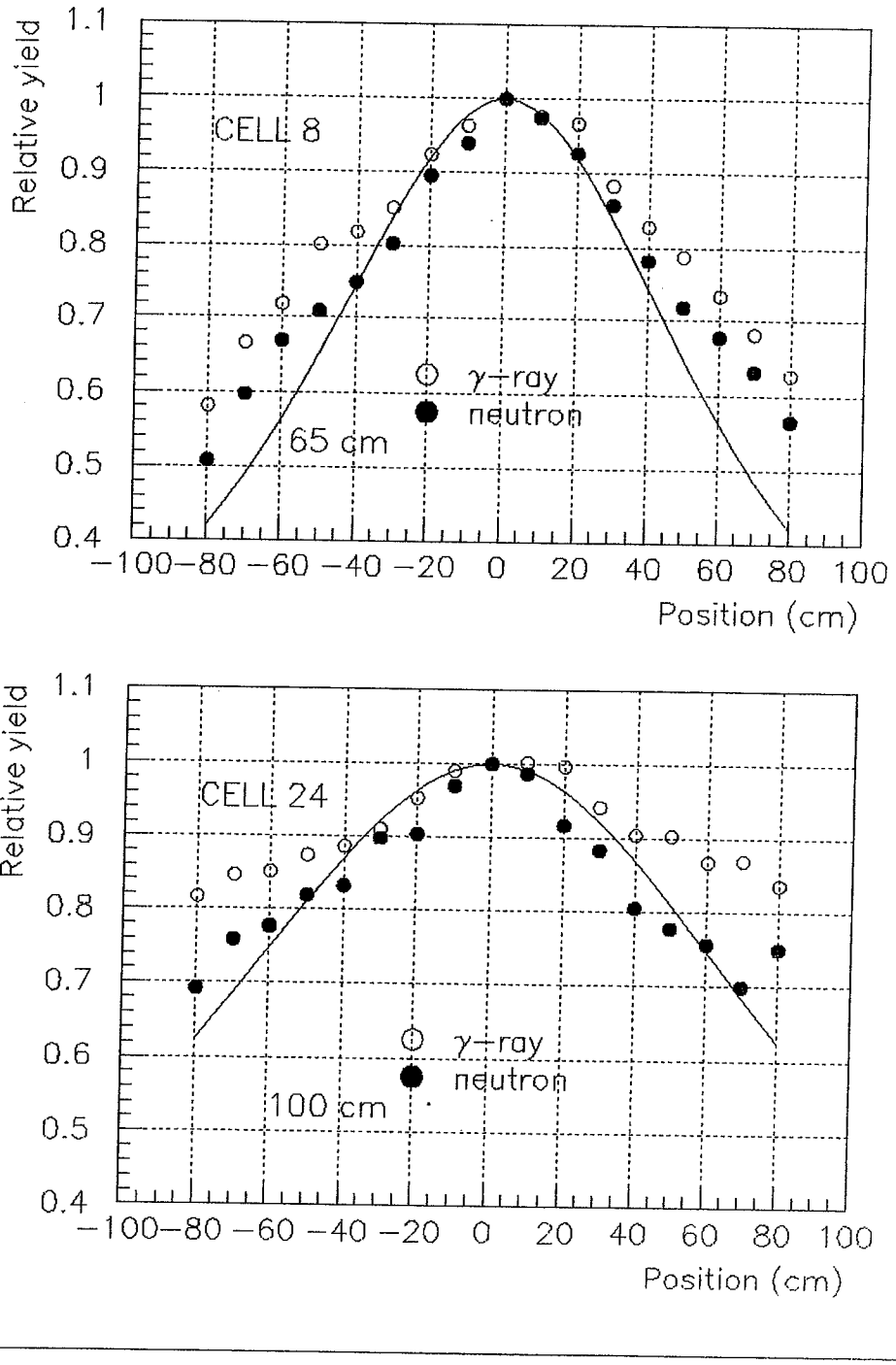
Relative yield
1.1
1
0.9
0.8
0.7
0.6
0.5
0.4
CELL 8
γ-ray
neutron
65 cm
−100 −80 −60 −40 −20 0 20 40 60 80 100
Position (cm)
Relative yield
1.1
1
0.9
0.8
0.7
0.6
0.5
0.4
CELL 24
γ-ray
neutron
100 cm
−100 −80 −60 −40 −20 0 20 40 60 80 100
Position (cm)

Fig. 23

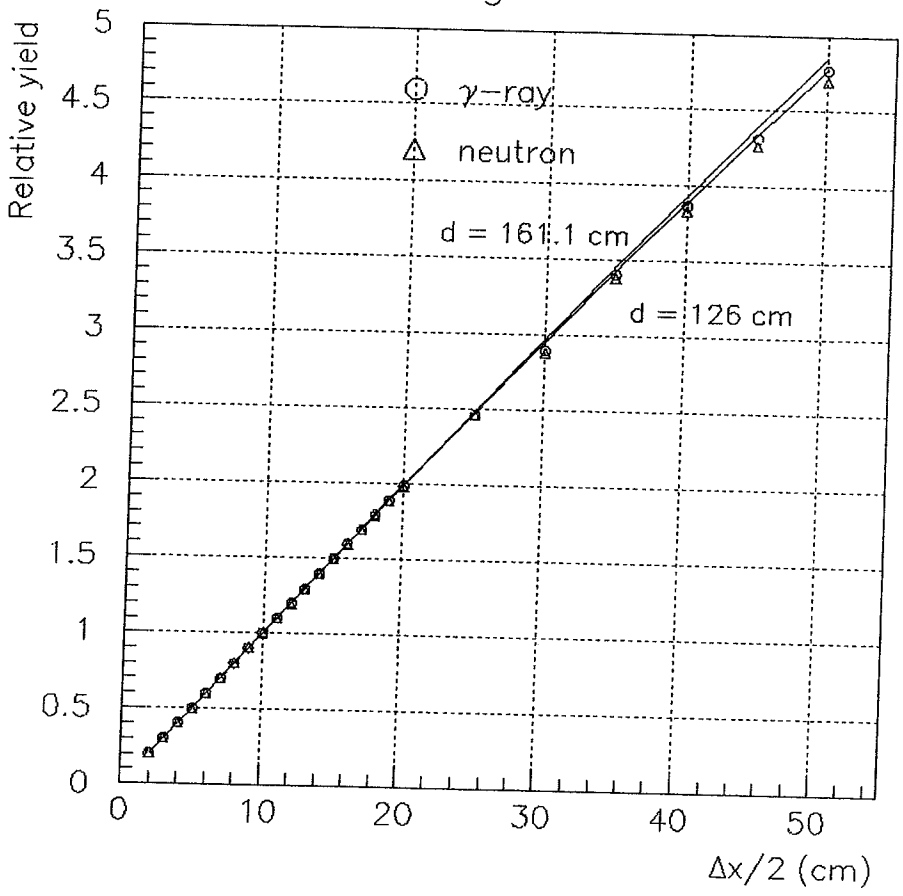
Relative yield
5
4.5
4
3.5
3
2.5
2
1.5
1
0.5
0
γ-ray
neutron
d = 161.1 cm
d = 126 cm
0
10
20
30
40
50
Δx/2 (cm)

Fig. 24

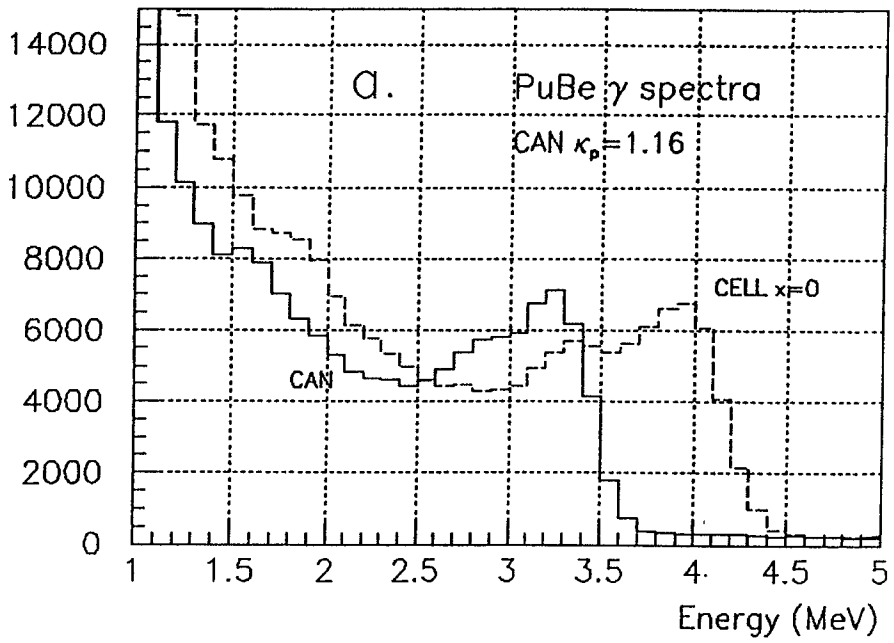
a.
PuBe γ spectra
CAN κ_p=1.16
CELL x=0
CAN
14000
12000
10000
8000
6000
4000
2000
0
1
1.5
2
2.5
3
3.5
4
4.5
5
Energy (MeV)

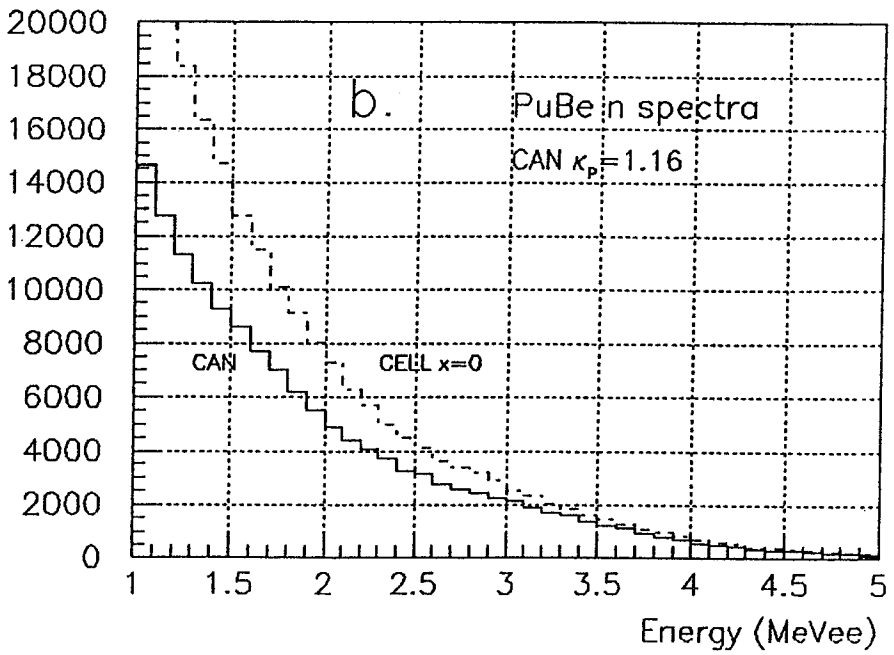
b.
PuBe n spectra
CAN κ_p=1.16
CAN
CELL x=0
20000
18000
16000
14000
12000
10000
8000
6000
4000
2000
0
1
1.5
2
2.5
3
3.5
4
4.5
5
Energy (MeVee)

Fig. 25a

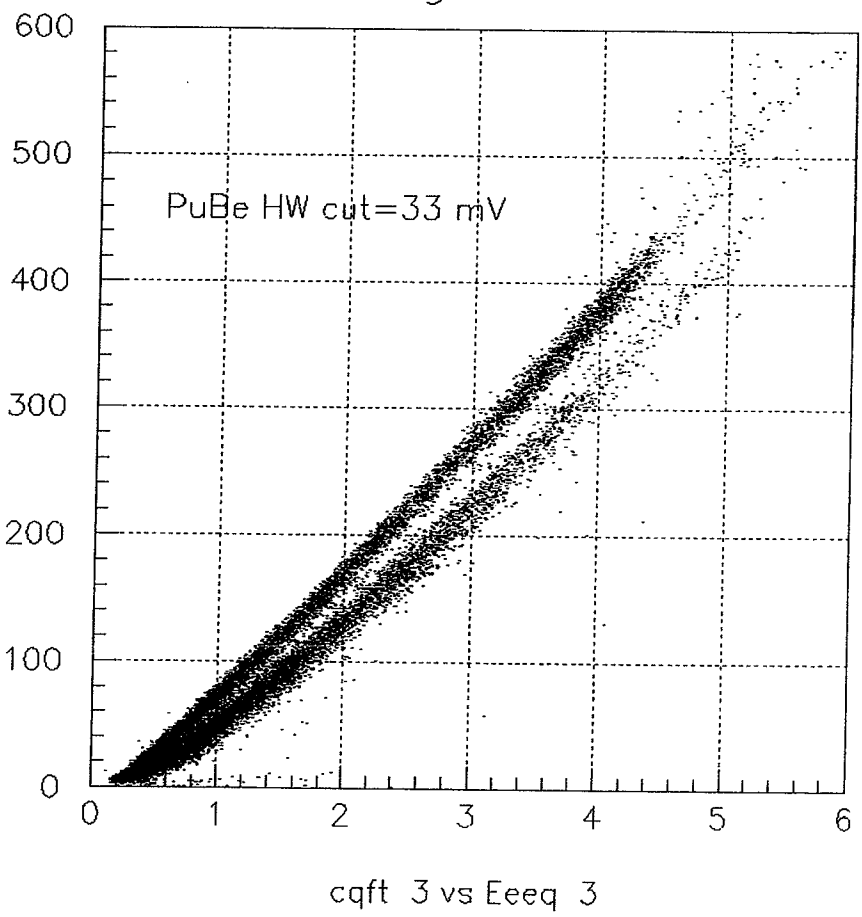
600
500
400
300
200
100
0
0
1
2
3
4
5
6
PuBe HW cut=33 mV
cqft 3 vs Eeeq 3

Fig. 25b

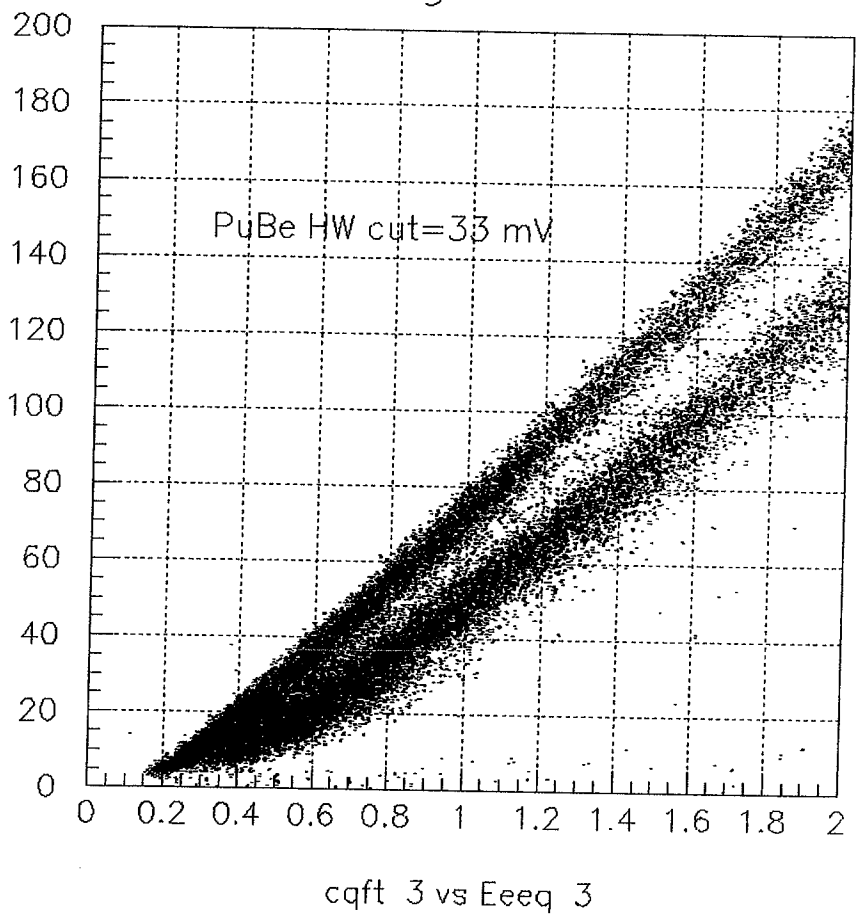
PuBe HW cut=33 mV
200
180
160
140
120
100
80
60
40
20
0
0
0.2
0.4
0.6
0.8
1
1.2
1.4
1.6
1.8
2
cqft 3 vs Eeeq 3

Fig. 26a–b

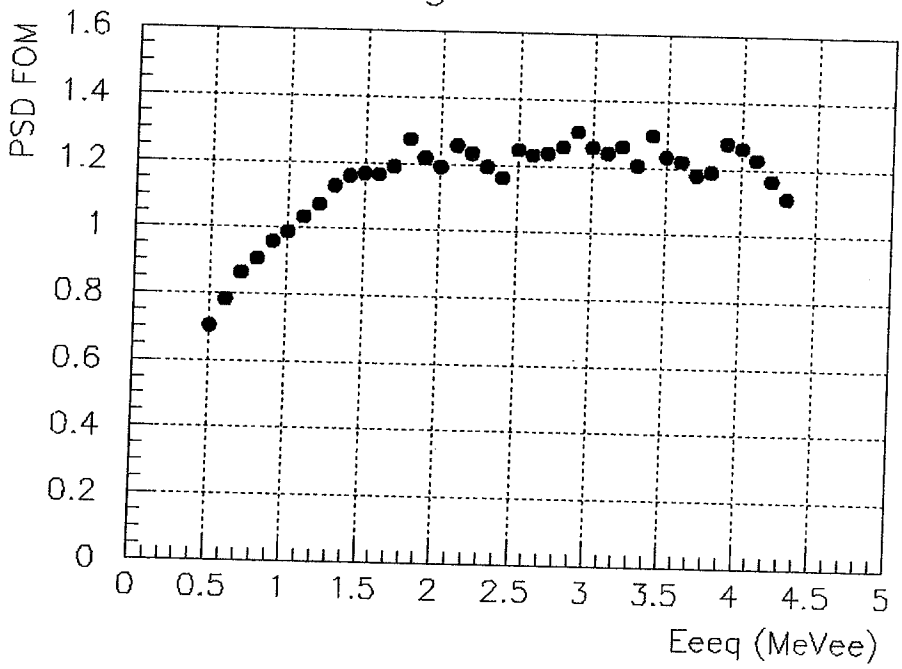
PSD FOM
1.6
1.4
1.2
1
0.8
0.6
0.4
0.2
0
0 0.5 1 1.5 2 2.5 3 3.5 4 4.5 5
Eeeq (MeVee)

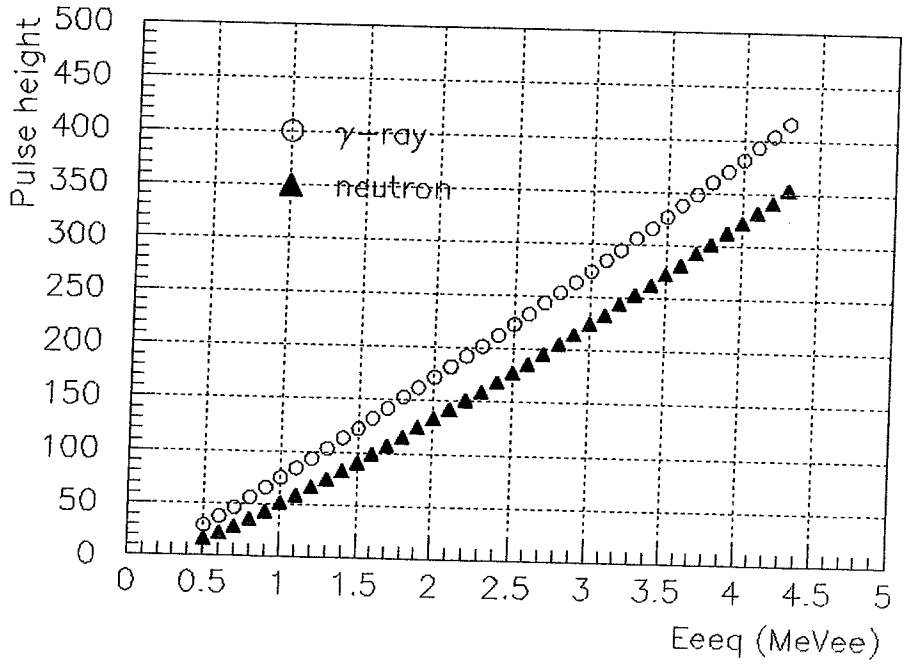
Pulse height
500
450
400
350
300
250
200
150
100
50
0
γ-ray
neutron
0 0.5 1 1.5 2 2.5 3 3.5 4 4.5 5
Eeeq (MeVee)

Fig. 26c

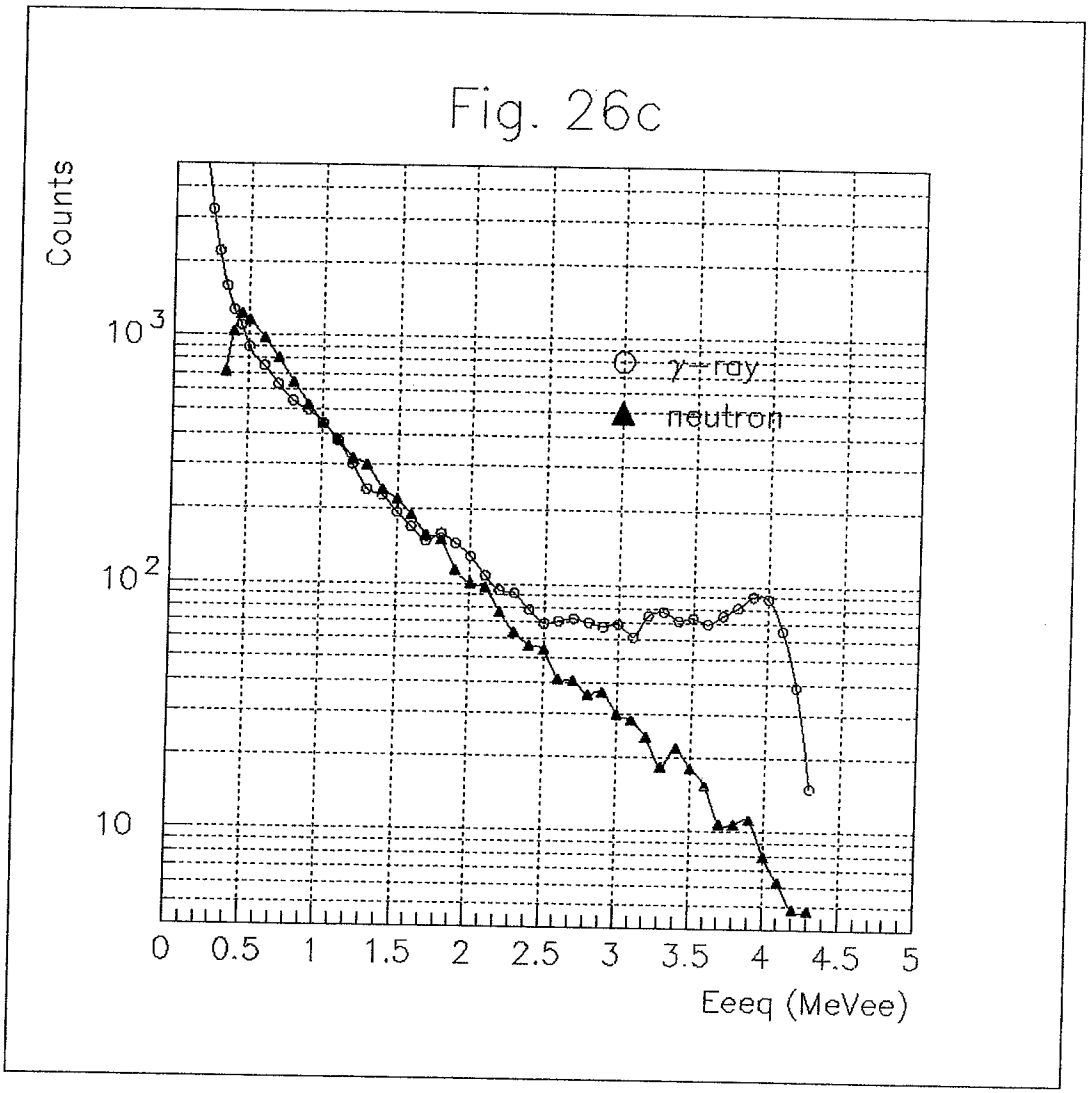
Counts
10^3
10^2
10
γ-ray
neutron
0
0.5
1
1.5
2
2.5
3
3.5
4
4.5
5
Eeeq (MeVee)

Fig. 27

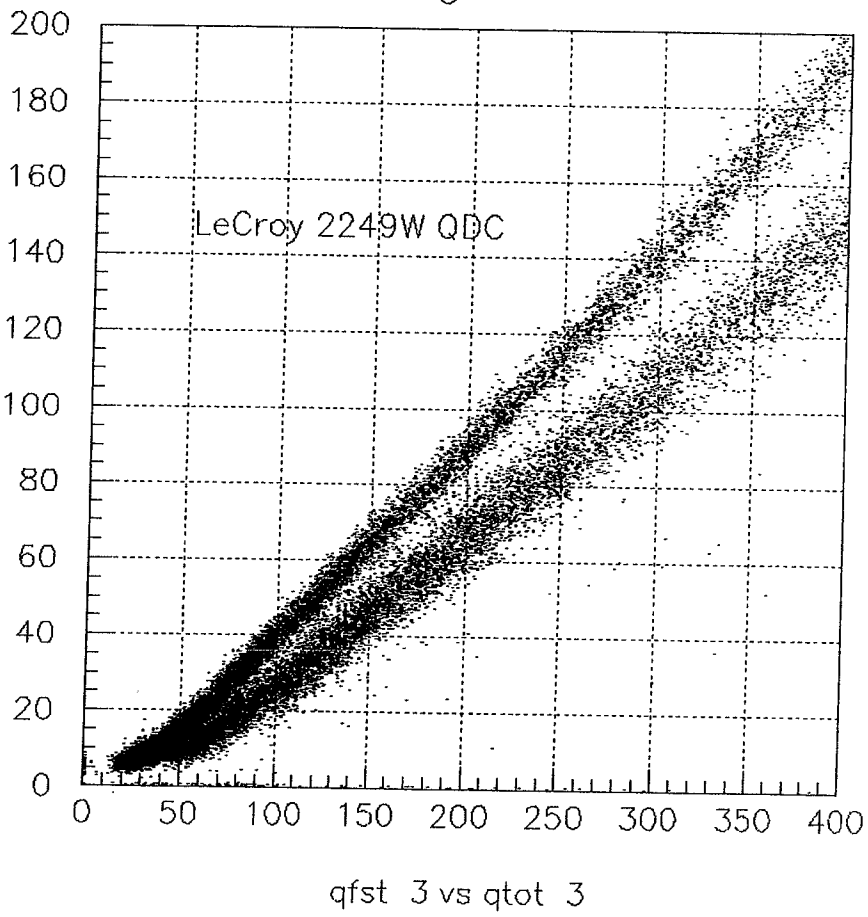
LeCroy 2249W QDC
200
180
160
140
120
100
80
60
40
20
0
0
50
100
150
200
250
300
350
400
qfst 3 vs qtot 3

Fig. 28

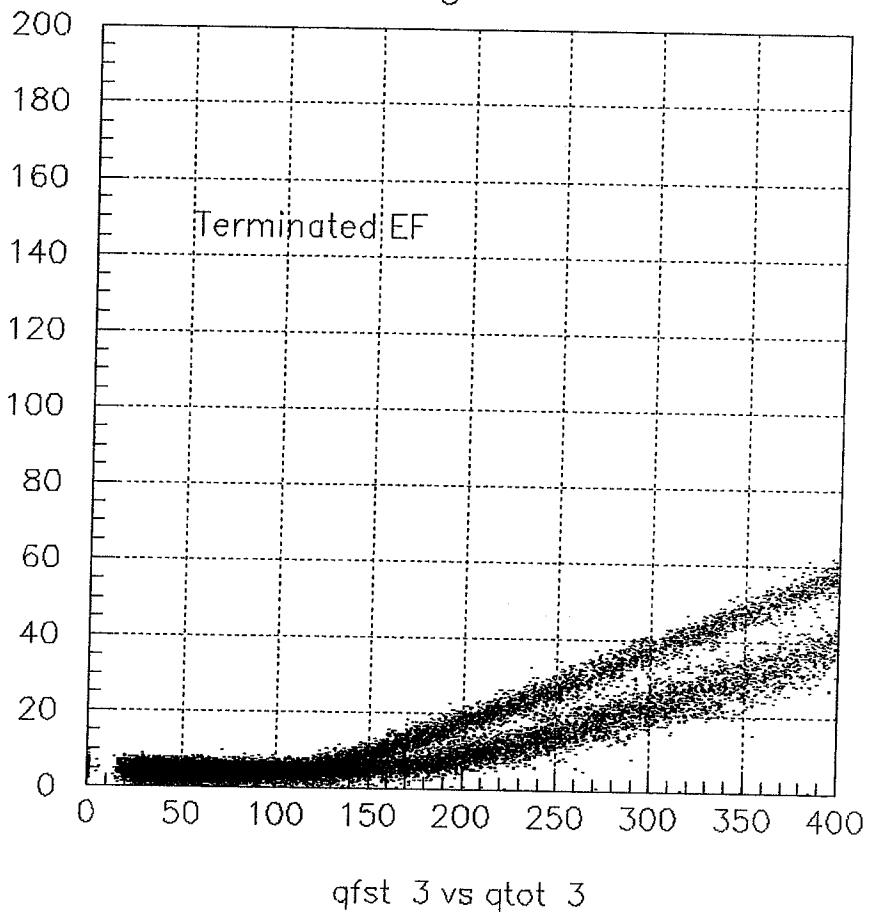
Terminated EF
200
180
160
140
120
100
80
60
40
20
0
0
50
100
150
200
250
300
350
400
qfst 3 vs qtot 3

Fig. 29

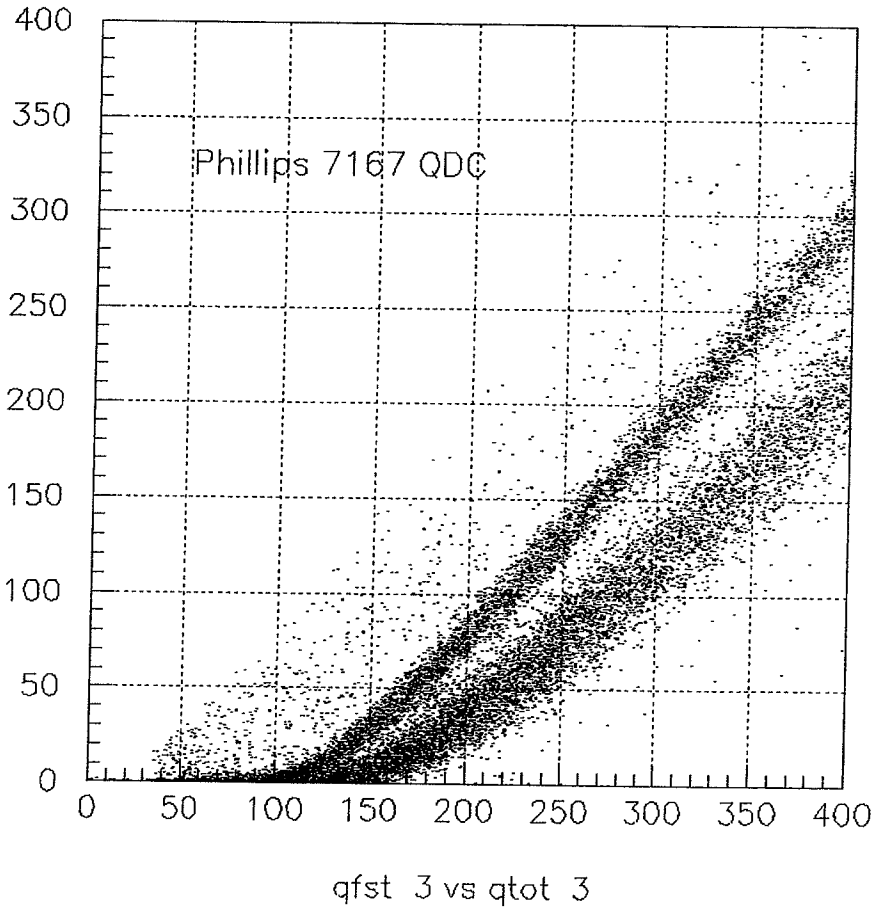
Phillips 7167 QDC
400
350
300
250
200
150
100
50
0
0
50
100
150
200
250
300
350
400
qfst 3 vs qtot 3

Fig. 30

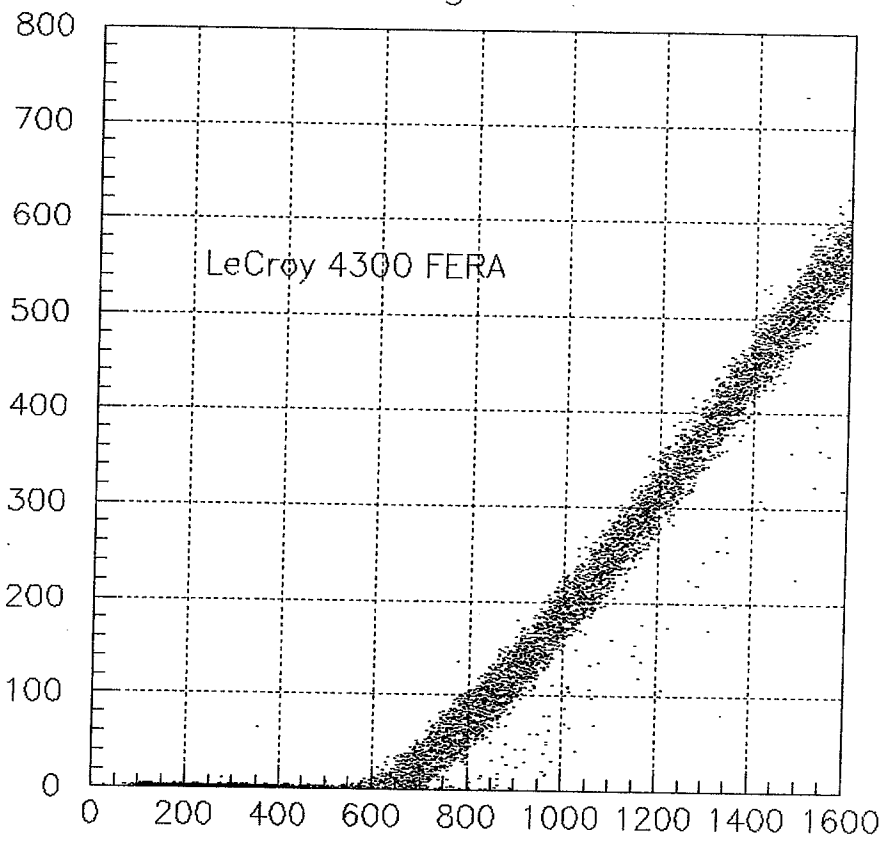
800
700
600
500
400
300
200
100
0
LeCroy 4300 FERA
0
200
400
600
800
1000
1200
1400
1600
qatt 3 vs qtot 3

Fig. 31

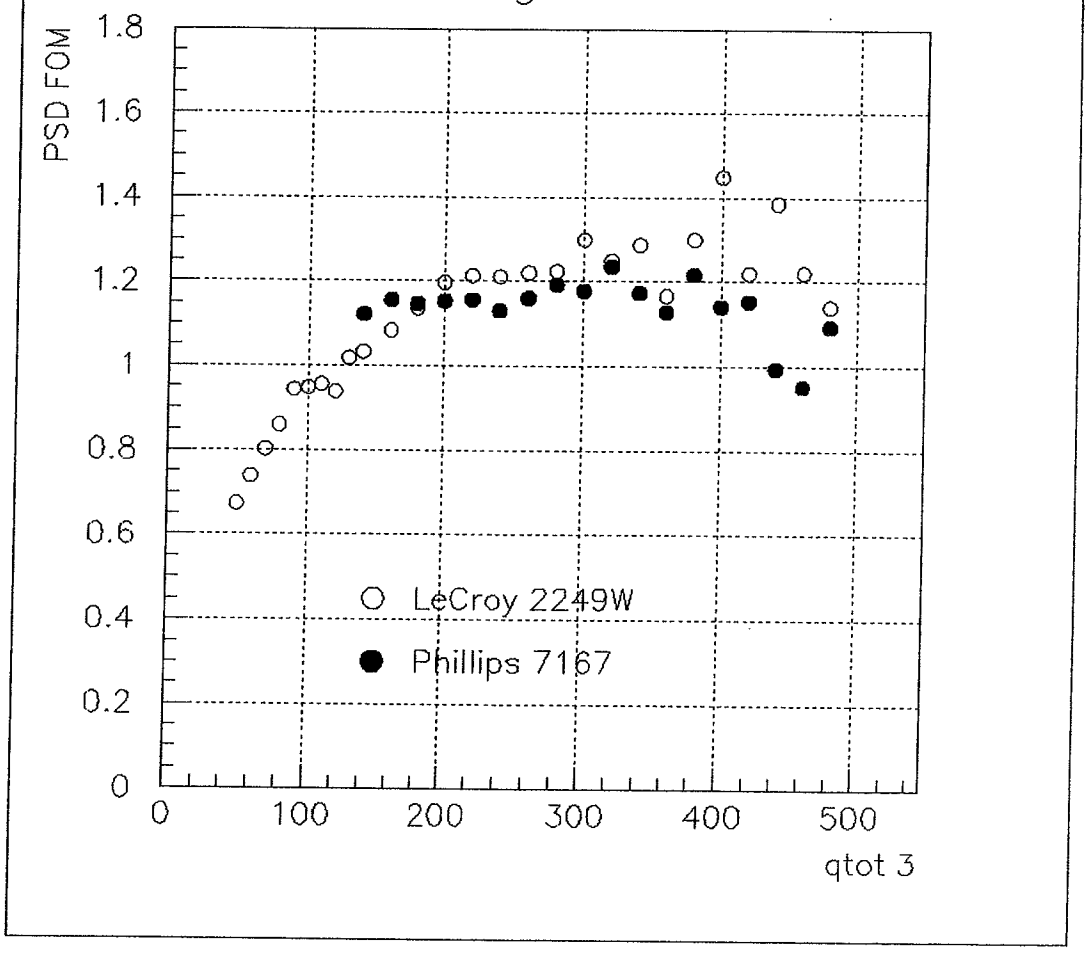
PSD FOM
1.8
1.6
1.4
1.2
1
0.8
0.6
0.4
0.2
0
0
100
200
300
400
500
qtot 3
LeCroy 2249W
Phillips 7167

Fig. 32

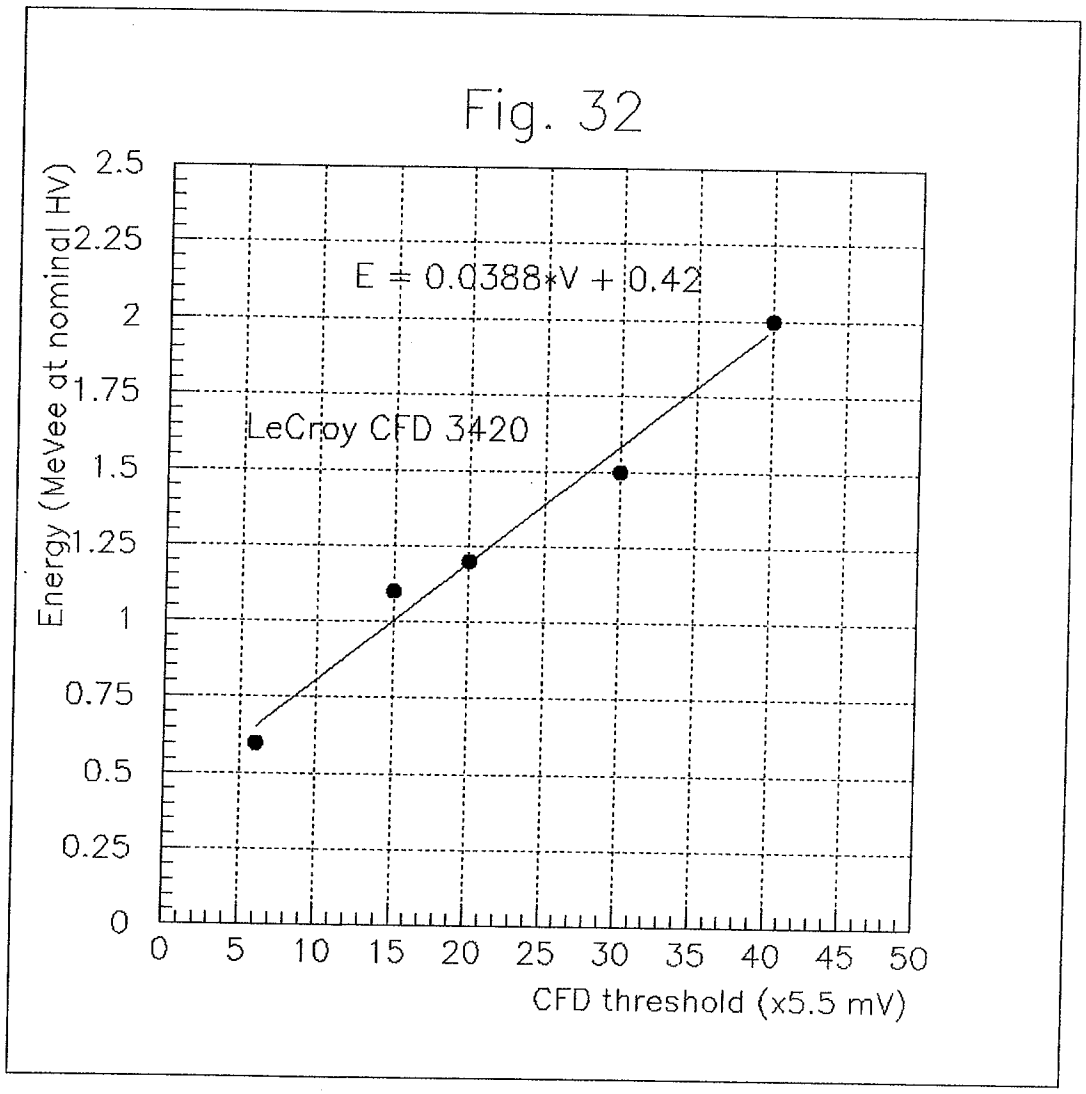
Energy (MeVee at nominal HV)
2.5
2.25
2
1.75
1.5
1.25
1
0.75
0.5
0.25
0
E = 0.0388*V + 0.42
LeCroy CFD 3420
0
5
10
15
20
25
30
35
40
45
50
CFD threshold (x5.5 mV)

Fig. 33

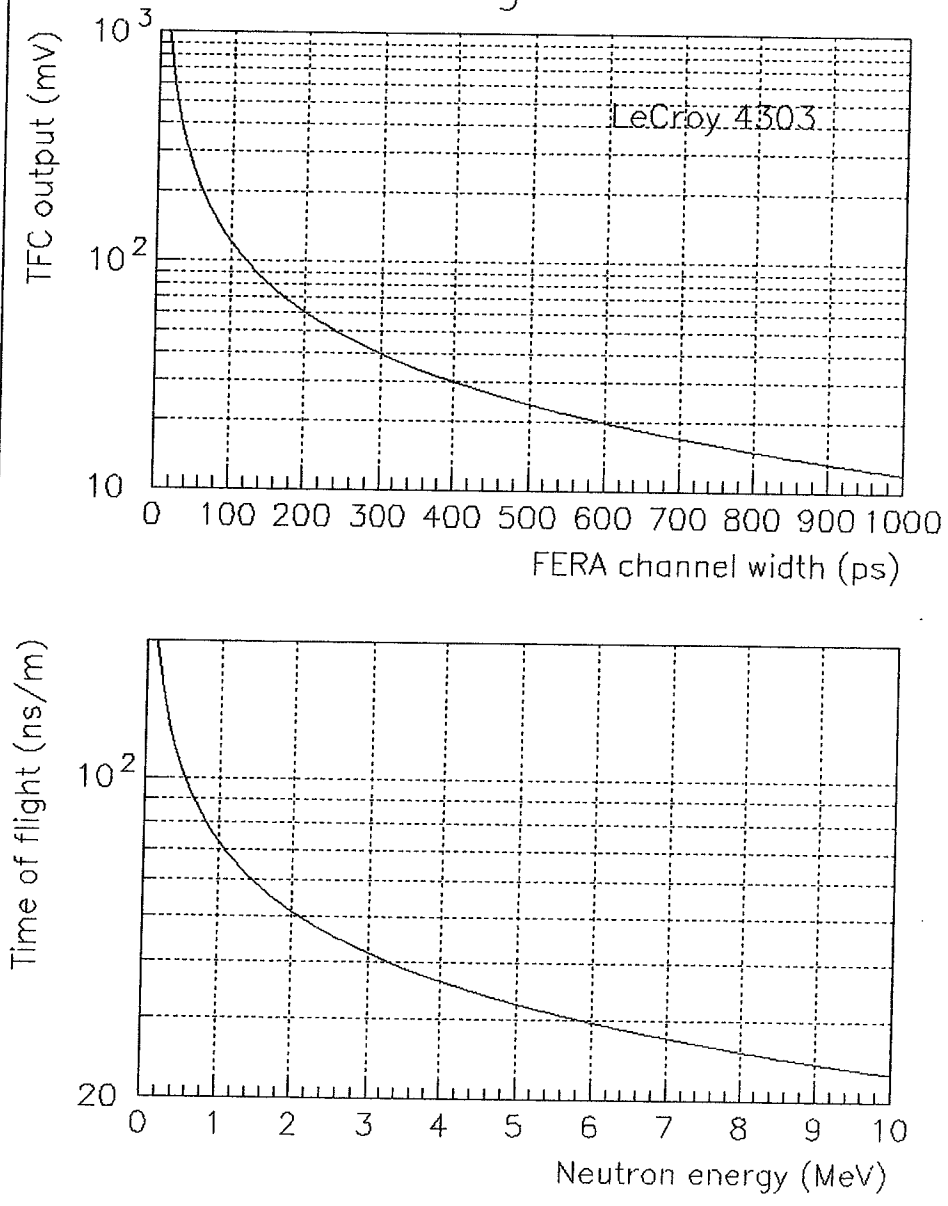
TFC output (mV)
10^3
10^2
10
LeCroy 4303
0 100 200 300 400 500 600 700 800 900 1000
FERA channel width (ps)
Time of flight (ns/m)
10^2
20
0 1 2 3 4 5 6 7 8 9 10
Neutron energy (MeV)